J. Fluid Mech. (2012), *vol.* 701, *pp.* 430–459. © Cambridge University Press 2012
doi:10.1017/jfm.2012.171

Non-normal dynamics of time-evolving co-rotating vortex pairs

X. Mao[1,2]†, S. J. Sherwin[1] and H. M. Blackburn[2]

[1] Department of Aeronautics, Imperial College London, South Kensington SW7 2AZ, UK

[2] Department of Mechanical and Aerospace Engineering, Monash University, 3800, Australia

(Received 12 March 2011; revised 26 February 2012; accepted 5 April 2012;
first published online 16 May 2012)

Transient energy growth of disturbances to co-rotating pairs of vortices with axial core flows is investigated in an analysis where vortex core expansion and vortex merging are included by adopting a time-evolving base flow. The dynamics of pairs are compared with those of individual vortices in order to highlight the effect of vortex interaction. Three typical vortex pair cases are studied, with the pairs comprised respectively of individually inviscidly unstable vortices at the streamwise wavenumber that maximizes the individual instabilities, viscously unstable vortices also at the streamwise wavenumber maximizing the individual instabilities and asymptotically stable vortices at streamwise wavenumber zero. For the inviscidly unstable case, the optimal perturbation takes the form of a superposition of two individual helical unstable modes and the optimal energy growth is similar to that predicted for an individual inviscid unstable vortex, while where the individual vortices are viscously unstable, the optimal disturbances within each core have similar spatial distributions to the individually stable case. For both of these cases, time horizons considered are much lower than those required for the merger of the undisturbed vortices. However, for the asymptotically stable case, large linear transient energy growth of optimal perturbations occurs for time horizons corresponding to vortex merging. Linear transient disturbance energy growth exhibited by pairs in this stable case is two to three orders of magnitude larger than that for a corresponding individual vortex. The superposition of the perturbation and the base flow shows that the perturbation has a displacement effect on the vortices in the base flow. Direct numerical simulations of stable pairs seeded by optimal initial perturbations have been carried out and acceleration/delay of vortex merging associated with a dual vortex meandering and vortex breakup related to axially periodic acceleration and delay of vortex merging are observed. For axially invariant cases, the sign of perturbation has an effect, as well as magnitude; the sign dependence relates to whether or not the perturbation adds to or subtracts from the swirl of the base flow. For a two-dimensional perturbation that adds to the swirl of the base flow, seeding with the linear optimal disturbance at a relative energy level 1×10^{-4} induces the pair to move towards each other and approximately halves the time required for merger. Direct numerical simulation shows that the optimal three-dimensional perturbation can induce the vortex system to break up before merging occurs, since the two-dimensional nature of vortex merging is broken by the development of axially periodic perturbations.

Key words: absolute/convective instability, vortex instability, vortex interactions

† Email address for correspondence: maoxuerui@sina.com

https://doi.org/10.1017/jfm.2012.171 Published online by Cambridge University Press

1. Introduction

Large aircraft in landing and take-off configurations generate strong multiple trailing vortex systems. In the near field, the trailing vortex sheet quickly rolls up and detaches from the wing tips and outer flap tips to form a set of discrete co-rotating vortices on each semi-span, which subsequently merge and form a pair of counter-rotating vortices downstream of the wing over a distance of 5–10 wing spans (Meunier, Le Dizès & Leweke 2005). These vortex systems may persist over long times before finally diffusing, and can impose potentially dangerous rolling moments on any following aircraft that encounters them (Crouch 2005). Airport safety regulations impose additional delays between aircraft movements in order to mitigate such events, and much of the motivation for studying dynamics and stability of trailing vortex wake systems stems from desire to increase airport utilization factors, especially for large aircraft.

Consideration of the dynamics of equal-strength vortex pairs is complicated by the large variety of behaviours that may be encountered. At finite Reynolds numbers, individual vortices expand and weaken with time owing to viscous diffusion, although at high Reynolds numbers this effect is comparatively slow and quasi-steady analyses may be made of the initial dynamics. On the basis of such an analysis, individual vortices of a pair may be found asymptotically unstable to a variety of mechanisms, as discussed, for example, by Heaton (2007*b*). Counter-rotating pairs are subject to the long-wavelength Crow instability (Crow 1970), a mechanism shown to be stable in the case of co-rotating pairs (Jiménez 1975). At shorter axial wavelengths, elliptic asymptotic instabilities (Kerswell 2002) of either co-rotating or counter-rotating pair systems can also arise where each vortex is distorted by the strain field of the other such that sectional streamlines become elliptical in shape. Transient as opposed to asymptotic dynamics of pairs may be significant, especially those associated with vortex merging which occurs only for co-rotating vortex pairs. An examination of optimal transient perturbations in quasi-steady counter-rotating pairs may be found in Donnadieu *et al.* (2009). Studies of transient dynamics of co-rotating pairs have thus far been confined to either direct numerical simulation (DNS), typically two dimensional, or conducted experimentally (see the review by Meunier *et al.* 2005, for discussion of both types). We are not aware of any existing study, quasi-steady or otherwise, that considers optimal transient dynamics of co-rotating pairs. The present work seeks to provide an introductory examination of this area, focusing most attention on cases where merging occurs in the base flow and so quasi-steady approximations are invalid.

In the remainder of this section we first consider the Batchelor model of the individual vortices used to initialize our base flows, and the asymptotic and transient behaviours expected of these vortices when considered individually (and, typically, on the basis of quasi-steady analysis). We briefly discuss elliptic asymptotic instability of pairs of such vortices, both co- and counter-rotating, and transient growth of counter-rotating pairs. We examine previous observations of vortex merging both for two-dimensional cases and in experiments where elliptic instability may contribute to the event. Finally, we outline and justify the approach to be taken for our investigation of optimal transient dynamics of co-rotating vortex pairs.

Trailing vortices often involve axial core flow in addition to swirl. A simple model that allows for both axial core flow and swirl and which for an isolated vortex satisfies the incompressible Navier–Stokes equations is provided by the Batchelor

https://doi.org/10.1017/jfm.2012.171 Published online by Cambridge University Press

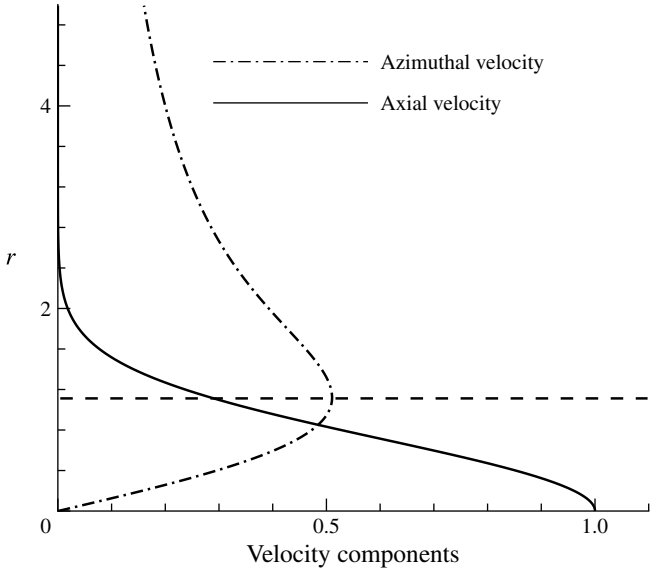


FIGURE 1. Radial profiles of axial and azimuthal velocity components for an individual Batchelor vortex at swirl strength $q = 0.8$, time $t = 0$ and radial length parameter $a(0) = 1$. Maximum azimuthal velocity is obtained at $r = 1.12091$, indicated by dashed line.

vortex (Batchelor 1964), defined in cylindrical coordinates (z, r, θ) by

$$(u_z, u_r, u_\theta)(r, t) = (a^{-2}\exp(-r^2/a^2), 0, qr^{-1}[1 - \exp(-r^2/a^2)]), \tag{1.1}$$

where $a(t) = (1 + 4t/Re)^{1/2}$ represents the viscous diffusion of the radius of the vortex core and q denotes the swirl strength. Here Re denotes the Reynolds number, defined as $Re = \Delta U R_0/\nu$, where ΔU is the dimensional velocity excess in the core of each individual vortex, R_0 is the radius of an individual vortex core at time $t = 0$ and ν is the kinematic viscosity. This model is adopted in what follows as the basis of individual vortex initial conditions, taken at time $t = 0$. Profiles of axial and azimuthal velocity components of a Batchelor vortex at time $t = 0$ and with $q = 0.8$ are shown in figure 1; we observe that the maximum azimuthal velocity occurs at $r = 1.12091$. As $q \to \infty$, axial flow becomes negligible and the Lamb–Oseen vortex model is approached.

We note that owing to viscous diffusion, the radial size of a Batchelor vortex increases with time, while velocities decay. Since the rate of these changes decreases as Reynolds numbers increase, quasi-steady analyses are generally reasonable for high initial Reynolds number studies. However, as will be discussed below, quasi-steady approaches cannot be appropriate to studies involving vortex merger, which is inherently unsteady, and also inherently a moderate-to-low Reynolds number phenomenon.

Asymptotic temporal behaviour of small perturbations to a quasi-steady individual vortex may be described by the eigenmodal form $\boldsymbol{u}'(z, r, \theta, t) = \hat{\boldsymbol{u}}(r)\exp[\sigma t + \mathrm{i}(kz + m\theta)]$, where the real and imaginary parts of σ denote the growth rate and frequency of the eigenmode $\hat{\boldsymbol{u}}$, respectively, k designates the streamwise wavenumber and m represents the azimuthal wavenumber. There are two major categories of asymptotic instabilities of perturbations to the Batchelor vortex: inviscid and viscous. We adopt the standard terminology (see e.g. Heaton 2007*b*) that an inviscid-type instability is

https://doi.org/10.1017/jfm.2012.171 Published online by Cambridge University Press

one for which the exponential growth rate σ increases to a positive finite value as $Re \to \infty$, while a viscous-type instability is one for which the growth rate tends to zero from above as $Re \to \infty$. Inviscid-type helical instabilities are very strong for $q < 1.5$, as investigated by Lessen & Paillet (1974), Lessen, Singh & Paillet (1974) and Mayer & Powell (1992) and stabilized for $q > 2.31$, as predicted by Stewartson & Brown (1985) and confirmed by Heaton (2007*a*): this means that inviscid mechanisms are not relevant to the asymptotic dynamics of Lamb–Oseen vortices. Viscous-type centre instabilities are much weaker, and occur at all values of swirl strength and high values of Reynolds number as numerically investigated by Khorrami (1991) and Fabre & Jacquin (2004) and theoretically predicted by Le Dizès & Fabre (2007).

Significant transient energy growth may occur when the individual vortex flow is asymptotically stable or weakly unstable, as demonstrated in quasi-steady studies of both the Lamb–Oseen vortex and the Batchelor vortex by Antkowiak & Brancher (2004), Pradeep & Hussain (2006) and Heaton & Peake (2007). The optimal perturbation is observed to be located in the region outside the vortex core and two typical mechanisms of transient growth are identified, one at $m = 1$ and the other at $m = 0$. Antkowiak & Brancher (2004) conjectured that at $m = \pm 1$ the transient effects are produced by resonance, which occurs if the out-of-core structure oscillates with the same frequency as a core wave. The same authors have identified another transient growth effect at $m = 0$, named as an 'anti-lift-up effect', which is associated with the emergence of azimuthal vorticity rolls emanating from azimuthal velocity streaks (Antkowiak & Brancher 2007). It has been demonstrated by Pradeep & Hussain (2006) and Heaton (2007*b*) via different approaches that the transient growth at $m = 0$ can be arbitrarily large when the radial length of the computational domain tends to infinity. Mao (2010) recently demonstrated that these two transient growth mechanisms can be ascribed to the non-normality of a continuous part of the spectrum, corresponding to asymptotically stable modes with energy lying outside the vortex core region. In this work, the resonance effect on transient growth was observed, while the anti-lift-up effect was not captured because the growth rate is small at $m = 0$ (even though the growth can reach an arbitrary large value over an infinite time interval) and therefore the waves with $m = 0$ did not produce optimal energy growth over the limited time horizon investigated.

Pairs of two-dimensional vortices of equal strength undergo motion as each vortex is advected (and strained) by the velocity field of its partner. In counter-rotating pairs, this results in a linear translation of the pair, while for co-rotating vortices, the pair rotates in the same sense as the individual vortices. In either case another parameter enters the problem, which is the dimensionless initial spacing of the pairs, typically supplied as $a(t)/b$. For pairs of vortices, there is no available analytical model which satisfies the Navier–Stokes equations, however for moderate-to-high Reynolds numbers a typical approach is to employ as initial condition the linear sum of two Batchelor vortices. Provided that the initial spacing is sufficient, this system rapidly evolves to a quasi-steady state which can be used for asymptotic stability analysis. In addition to the single-vortex instability mechanisms outlined above, new mechanisms relying on the interactions between two vortices come into play. For asymptotic instability of co-rotating pairs prior to merging, only the short-wavelength elliptic mechanism needs to be considered.

The short-wave elliptic instability for an individual vortex in an external imposed strain field was numerically studied by Tsai & Widnall (1976) and theoretically described by Moore & Saffman (1975) as the resonant interaction between the strain and Kelvin waves with azimuthal wavenumbers $m = \pm 1$. This elliptic instability has been well-documented by Kerswell (2002) and is also observed in the

https://doi.org/10.1017/jfm.2012.171 Published online by Cambridge University Press

co-rotating Lamb–Oseen vortex pair flow (Le Dizès & Laporte 2002; Meunier & Leweke 2005). As noted by Meunier *et al.* (2005), asymptotic elliptic instability arises in the co-rotating Lamb–Oseen pair system prior to merger for moderate Reynolds numbers, $Re > 2000$.

The study by Roy *et al.* (2008) examined asymptotic elliptic instability in the co-rotating Batchelor pair system at streamwise wavenumber $k > 1$ and high values of the swirl strength $q > 1.67$ where the inviscid instability is weak. Similar to the work of Lacaze, Ryan & Le Dizès (2007) on the counter-rotating system, a number of elliptic instabilities were observed, each corresponding to resonance between a pair of Kelvin modes differing by two in azimuthal wavenumber, and in both studies the $m = \pm 1$ sinuous modes of the Lamb–Oseen system were stabilized by the addition of axial flow owing to a breaking of a symmetry between the $m = -1$ and $m = 1$ Kelvin waves that is only present when there is no axial flow. As outlined in Roy *et al.* (2008), the elliptic instabilities of the co-rotating and counter-rotating Batchelor vortex systems are broadly similar, but the effect of Coriolis acceleration, present in the co-rotating case and absent in the counter-rotating case, is to shift the modes to somewhat lower axial wavenumbers and to give a general increase in amplification rates. For counter-rotating Lamb–Oseen pairs, a new oscillatory elliptic instability involving Kelvin waves with azimuthal wavenumbers $m = 0$ and $|m| = 2$ was recently addressed by Donnadieu *et al.* (2009), who also investigated the transient energy growth of disturbances to a counter-rotating vortex pair.

As time proceeds, the individual vortices in a two-dimensional pair gradually expand and weaken as the result of viscous diffusion. In the case of a two-dimensional system of co-rotating vortex pairs, the vortices rotate around their mutual centroid at an almost constant radius and speed until the core radius to spacing parameter reaches a critical value of approximately $a/b = 0.22$, regardless of the initial Reynolds number (Meunier *et al.* 2005). At this time, the merging process begins; the vortices are driven towards each other and rotation of the pair speeds up, until separate vortex cores can no longer be discerned and the merger is complete. The resulting single-vortex system then diffuses away. For the two-dimensional case, core velocities do not affect these dynamics. Elliptic instability (arising for $Re > 2000$ in the case of Lamb–Oseen co-rotating pairs) can have a strong influence on the merging process, initiating it earlier and producing a final turbulent vortex of larger core size after merging completes (Meunier *et al.* 2005). We note that the merging process, either two or three dimensional, is highly unsteady and hence is not suited to study via quasi-steady approaches.

The importance of vortex interactions and vortex core expansions in the dynamics of vortex systems suggests it is necessary to take into account the time dependence of the base flow and conduct dynamic analyses over the whole process of the vortex interaction until merging completes. Transient growth analysis is an ideal tool with which to study this problem but little attention has been paid to the non-normality of vortex systems in the unsteady evolution process. In the present paper, a co-rotating vortex pair is adopted as an example vortex system and transient dynamics in the expansion–merging process are investigated computationally. The choice of co-rotating rather than counter-rotating vortex pairs dictates that the individual vortices undergo rotation around their joint centroid rather than translation parallel to the plane of symmetry, which could require a much larger computational domain. In addition, most of the previous works on dynamics of vortex pairs have been concerned with vortex systems consisting of individually stable vortices. The system instability of vortex pairs consisting of asymptotically unstable vortices has not been fully understood. In our work, the dynamics of vortex pairs consisting either of individually

https://doi.org/10.1017/jfm.2012.171 Published online by Cambridge University Press

unstable vortices or individually stable vortices are investigated and compared with the dynamics of the individual vortices in order to help fill this gap. For the systems chosen, the asymptotic behaviour of the pairs (stable/unstable) is the same as for the individual vortices.

We first used $(Re, q) = (1000, 0.8)$, where the individual vortex has strong inviscid instability (Broadhurst 2007), in order to study the interaction of the pair's mutual strain field and the inviscid instability. The swirl strength $q = 0.8$ ensures that a helical-type instability is activated. Following this, we increase the swirl strength to $q = 2$ and change the Reynolds number to $Re = 3000$ so as to activate the viscous centre instability in each individual vortex (Fabre & Jacquin 2004). Here we chose a relatively high Reynolds number since this is essential for a viscous centre instability to be observed. Then we further increase the swirl strength to $q = 3$ to preclude asymptotic instabilities associated with individual vortices and focus on vortex interaction and merging. In this case we employ $Re = 100$ in order to ensure that the vortices merge within a relatively brief time interval. Since our Reynolds numbers are based on the maximum axial velocity and initial radius rather than, as is conventional for Lamb–Oseen vortices, on the circulation, we note that our Reynolds numbers may not be directly comparable to those cited in other studies. For example, in the scaling adopted by Meunier *et al.* (2005), the initial Reynolds number for this case is $2\pi \times q \times 100 = 1885$. While this Reynolds number may still seem somewhat low, it is relevant to the study of merger dynamics, since (with initial core spacings above those for commencement of merging) the system is close to the onset of merging, set approximately at the border between the end of the initial quasi-steady phase ('stage 1' in figure 5 of Meunier *et al.* 2005) and the merger-onset phase ('stage 2'). As noted by Meunier *et al.* (2005) the duration of two-dimensional mergers is almost independent of the initial Reynolds number of the pair. In the three-dimensional case which gives the largest transient growth during merging, the basic mechanism is identified as elliptic.

Following studies of linear transient growth, we turn to examine the influence of nonlinear effects on the transient dynamics of the asymptotically stable pair. It is found that while the growth of perturbations falls as their relative amplitude is increased, this decline is accompanied in the two-dimensional case by either an acceleration or delay of vortex merging, depending on the sign of the perturbation, and in the three-dimensional case when perturbation levels are large, by a break-up of the individual vortices of the pair prior to merging.

2. Problem definition

In what follows, the linear summation of two Batchelor vortices is used as an initial condition to generate base flows with time-evolving co-rotating vortex pairs. In Cartesian spatial coordinates (x, y, z), corresponding to transverse, vertical and axial directions respectively, the initial condition can be expressed as

$$U(t=0) = -\frac{q}{r_1^2}(y - y_1)[1 - \exp(-r_1^2)] - \frac{q}{r_2^2}(y - y_2)[1 - \exp(-r_2^2)] \tag{2.1a}$$

$$V(t=0) = \frac{q}{r_1^2}(x - x_1)[1 - \exp(-r_1^2)] + \frac{q}{r_2^2}(x - x_2)[1 - \exp(r_2^2)] \tag{2.1b}$$

$$W(t=0) = \exp(-r_1^2) + \exp(-r_2^2) \tag{2.1c}$$

where $r_1^2 = (x - x_1)^2 + (y - y_1)^2$, $r_2^2 = (x - x_2)^2 + (y - y_2)^2$ and (x_1, y_1) and (x_2, y_2) are the initial locations of the two individual vortex cores. We note that axial vorticity

https://doi.org/10.1017/jfm.2012.171 Published online by Cambridge University Press

of this combination has positive sign, although of course the choice is arbitrary. For the view orientations chosen for figures, individual vortices and pairs rotate with a counter-clockwise sense.

As noted in § 1, while each isolated Batchelor vortex satisfies the Navier–Stokes equations, the combined initial condition does not. However, when this initial condition is evolved via time integration, there is a quick relaxation process ($t < 0.01$) during which the vortices equilibrate with each other without changing shape significantly (Sipp, Jacquin & Cossu 2000). This relaxation process is explained using the damped Kelvin modes of each vortex by Le Dizès & Verga (2002). This rapid and small readjustment has been found to have negligible influence on the outcomes provided in the present work.

The initial coordinates of the two vortex centroids are $(x_1, y_1) = (-b/2, 0)$ and $(x_2, y_2) = (b/2, 0)$, where we have concentrated most attention on a dimensionless spacing $b = 6$. This initial spacing ensures that the individual vortices in each pair are not initially significantly distorted by their mutual strain field, and that the vortex system can merge over a relatively small time interval. In the individual vortex simulations used for purposes of comparison, the vortex centroid is located at $(x, y) = (-b/2, 0)$.

The problem to be examined is transient growth of optimal perturbations to the co-rotating vortex pair system. Base flows are taken to be time evolving, two dimensional with three velocity components. Perturbations are, in general, three dimensional with three velocity components with a Fourier decomposition in the axial coordinate (for which the base flows are homogeneous). The four dimensionless parameters to be considered are swirl strength q, Reynolds number Re, initial core spacing to radius ratio $a(0)/b$ and axial wavenumber k.

3. Transient growth methodology

Assuming the fluid to be Newtonian and the flow incompressible, the relevant equations of motion are the incompressible Navier–Stokes equations:

$$\partial_t \boldsymbol{u} = -\boldsymbol{u} \cdot \boldsymbol{\nabla} \boldsymbol{u} - \boldsymbol{\nabla} p + Re^{-1} \nabla^2 \boldsymbol{u}, \quad \boldsymbol{\nabla} \cdot \boldsymbol{u} = 0, \tag{3.1}$$

where $\boldsymbol{u}$ is a velocity vector field and p is a modified pressure, all considered in a spatial domain Ω. Decomposing the flow field into the sum of a base flow and a perturbation, $\boldsymbol{u} = \boldsymbol{U} + \boldsymbol{u}'$, $p = P + p'$, inserting into (3.1), and retaining only terms linear in the perturbation, one obtains the linearized Navier–Stokes (LNS) equations

$$\partial_t \boldsymbol{u}' = -\boldsymbol{U} \cdot \boldsymbol{\nabla} \boldsymbol{u}' - \boldsymbol{u}' \cdot \boldsymbol{\nabla} \boldsymbol{U} - \boldsymbol{\nabla} p' + Re^{-1} \nabla^2 \boldsymbol{u}', \quad \boldsymbol{\nabla} \cdot \boldsymbol{u}' = 0. \tag{3.2}$$

As noted in § 2, the perturbation is further decomposed in the axial coordinate direction, such that $\boldsymbol{u}' = \tilde{\boldsymbol{u}} \exp(\mathrm{i}kz) + \text{c.c.}$, where k is the axial wavenumber. In the linear case each such Fourier mode will evolve independently. Spatial distributions of eigenmode and perturbation vorticity shown in the figures to follow are derived from two-dimensional Fourier modes $\tilde{\boldsymbol{u}}$.

We adopt a direct approach to computing initial conditions that lead to optimal transient growth, based on sequential time integration of the linearized and adjoint Navier–Stokes equations (Barkley, Blackburn & Sherwin 2008; Blackburn, Barkley & Sherwin 2008). As is typical, we define transient growth with respect to the energy norm of the perturbation flow, derived from the L_2 inner product

$$2E(\boldsymbol{u}') = (\boldsymbol{u}', \boldsymbol{u}') \equiv \int_\Omega \boldsymbol{u}' \cdot \boldsymbol{u}' \, \mathrm{d}V, \tag{3.3}$$

https://doi.org/10.1017/jfm.2012.171 Published online by Cambridge University Press

where E is the kinetic energy per unit mass of a perturbation, integrated over the full domain. If the initial perturbation $\boldsymbol{u}'(0)$ is taken to have unit norm, then the transient energy growth over time horizon τ is

$$\frac{E(\tau)}{E(0)} = \big(\boldsymbol{u}'(\tau), \boldsymbol{u}'(\tau)\big) = \big(\mathscr{A}(\tau)\boldsymbol{u}'(0), \mathscr{A}(\tau)\boldsymbol{u}'(0)\big) = \big(\boldsymbol{u}'(0), \mathscr{A}^*(\tau)\mathscr{A}(\tau)\boldsymbol{u}'(0)\big)\,, \quad (3.4)$$

where $\mathscr{A}(\tau)$ is the forward state transition operator whose action is obtained by integrating the LNS equations (3.2) over interval τ; $\mathscr{A}^*(\tau)$ is the adjoint of $\mathscr{A}(\tau)$, whose action is obtained by integrating the adjoint LNS equations

$$-\partial_t \boldsymbol{u}^* = \boldsymbol{U}\cdot\nabla\boldsymbol{u}^* - \boldsymbol{u}^*\cdot(\nabla\boldsymbol{U})^{\mathrm{T}} - \nabla p^* + Re^{-1}\nabla^2\boldsymbol{u}^* \quad \text{with } \nabla\cdot\boldsymbol{u}^* = 0 \quad (3.5)$$

backwards over the interval τ. The action of the symmetric operator $\mathscr{A}^*(\tau)\mathscr{A}(\tau)$ on $\boldsymbol{u}'$ over the time horizon τ is obtained by sequential time integration of $\mathscr{A}(\tau)$ and $\mathscr{A}^*(\tau)$, starting with $\boldsymbol{u}'$ as an initial condition. The optimal energy growth over all possible initial conditions for a specific time horizon, $G(\tau)$, can be interpreted as the largest eigenvalue of the operator $\mathscr{A}^*(\tau)\mathscr{A}(\tau)$ (equivalently the square of the leading singular value of $\mathscr{A}(\tau)$) and this leading eigenvalue is calculated via an Arnoldi method that relies on repeated application of the joint operator. The global maximum is denoted by $G_{max} = \max_\tau G(\tau)$. Perturbation velocity boundary conditions are $\boldsymbol{u}' = \boldsymbol{u}^* = 0$.

The base flow data are time dependent and updated at every time step by reconstruction from a moderate number of precomputed time slices. We have investigated two interpolation methods to reconstruct the base flow: cubic spline interpolation and four-point-Lagrange (local cubic) interpolation. Both methods deliver similar results but the first needs all of the slices at every time step and makes the base flow reconstruction the dominant work component. Local cubic interpolation is much cheaper while delivering formally the same order of accuracy in time as global cubic spline interpolation, so four-point-Lagrange interpolation was adopted. For convenience and speed all of the base flow data were retained in core memory but only four slices are actually needed in core to compute the interpolant at any instant so the majority could be kept in slower memory if required. The same base flow reconstruction methodology was applied in Mao, Sherwin & Blackburn (2011).

4. Discretization and validation, base flow calculations

The governing equations are discretized via quadrilateral spectral elements with nodal tensor-product expansion bases. A second-order backward-difference time-splitting scheme with equal-order interpolation of velocity and pressure (Karniadakis, Israeli & Orszag 1991; Guermond, Minev & Shen 2006) is used for time integration with time step $\Delta t = 0.005$. Where we have employed contour plots of solution axial vorticity component to illustrate results, this was computed in post-processing via collocation differentiation.

The mesh used for base flow, eigenmodal, transient growth and DNS calculations is shown in figure 2. Spectral elements are concentrated in the approximately circular region in which energy of the vortex pair is concentrated.

To validate our implementation, we compute the exponential temporal growth rate σ for an eigenmodal perturbation to a time-invariant base flow, and examine both spatial convergence with respect to the expansion basis polynomial order P and comparison with other published results. The growth rate is calculated using a time stepper approach, using an Arnoldi method based on repeated integration of the LNS equations (3.2) over a small time interval, as outlined in Tuckerman & Barkley (2000)

https://doi.org/10.1017/jfm.2012.171 Published online by Cambridge University Press

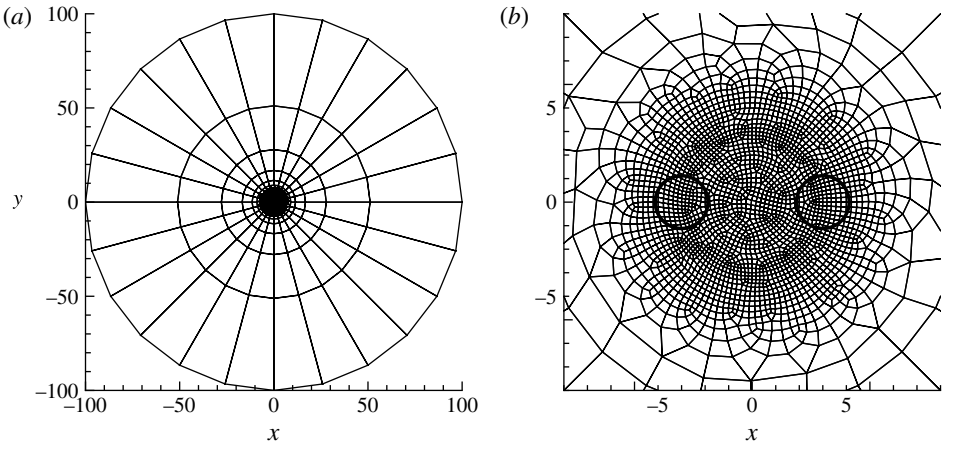


FIGURE 2. Mesh used in the base flow calculation, transient growth and DNS studies for both individual vortex and co-rotating vortex pair simulations: (*a*) entire domain; (*b*) detailed view, with two circles to represent initial core regions in the vortex pair flow.

Reynolds number (Re)	100	1000	10 000
Swirl strength (q)	0.622	0.771	0.776
Axial wavenumber (k)	1.108	1.659	1.664
σ, $P=2$	0.18109	0.32419	0.35106
σ, $P=3$	0.18118	0.32446	0.35134
σ, $P=4$	0.18118	0.32446	0.35135
σ, $P=5$	0.18118	0.32446	0.35136
σ, $P=6$	0.18118	0.32446	0.35135
σ (Fabre & Jacquin 2004)	0.1812	0.3245	0.3514

TABLE 1. Study of convergence with respect to basis function polynomial order P for the asymptotic growth rate σ of a perturbation to an individual Batchelor vortex, with validation against the results of Fabre & Jacquin (2004).

and Barkley *et al.* (2008). The data computed using the present method and mesh are compared with the published results of Fabre & Jacquin (2004) in table 1. We can see that the two sets of data agree very well. The growth rate for $Re = 10\,000$ converges to four significant figures at $P = 4$, where P is the polynomial order of the used to construct tensor-product spectral element basis functions. Both $P = 4$ and $P = 5$ have been adopted for subsequent calculations.

Since the axial velocity and vorticity of the base flows satisfy the same advection–diffusion equation, it would be sufficient to compute just one of these in order to generate a three-component base flow (Donnadieu *et al.* 2009), but in the present work the three velocity components are evolved simultaneously via two-dimensional DNS.

Development of a typical base flow is illustrated in figure 3. Each individual vortex rotates around the centroid of the pair and is elliptically deformed owing to the strain field generated by the other vortex (figure 3*b*). Owing to viscous diffusion, the vortex cores expand with increasing time (figure 3*c*). When the separation distance falls below the merging threshold, the two vortices become closer and closer and finally

https://doi.org/10.1017/jfm.2012.171 Published online by Cambridge University Press

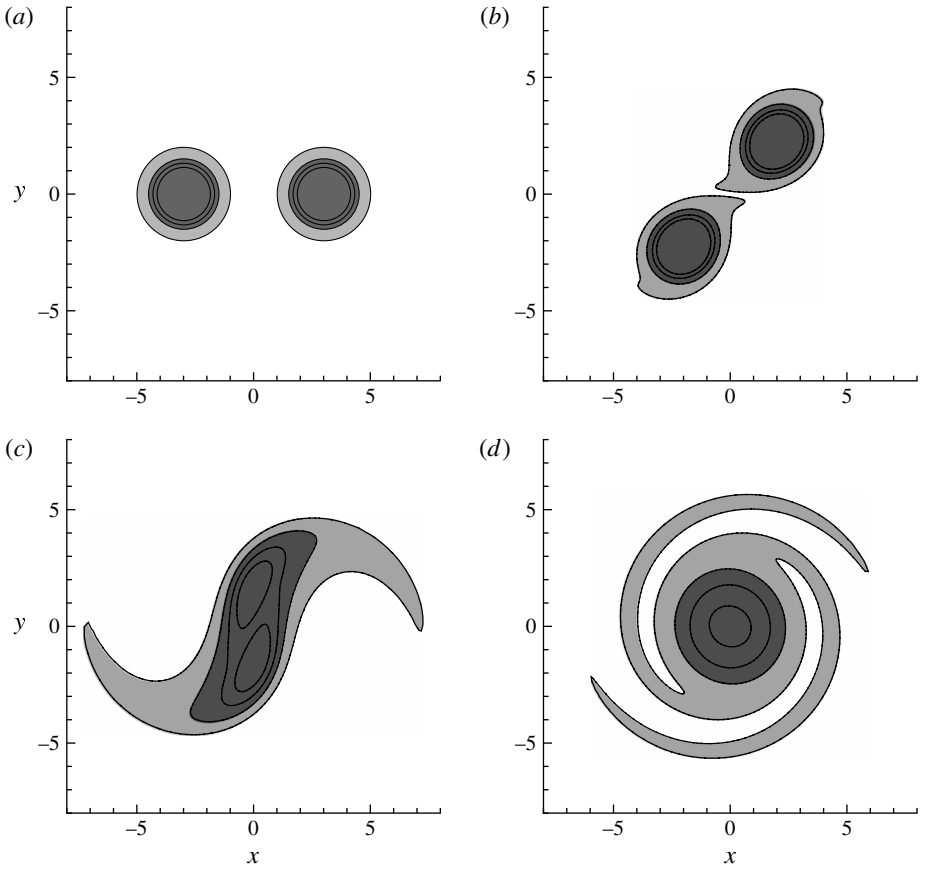


FIGURE 3. Development of axial vorticity contours of the co-rotating vortex base flow from the initial condition as described by (2.1). Initial Reynolds number $Re = 100$, core spacing $b = 6$, swirl strength $q = 3$: (*a*) $t = 0$; (*b*) $t = 5$; (*c*) $t = 39$; (*d*) $t = 60$. Contour levels range from $\zeta_z = 0$ to 1.6 and the same levels are used in all of the subplots. Darker shading indicates higher vorticity level.

merge to form a single vortex surrounded by rotating arms connected to the core (figure 3*d*).

In the transient growth study, the unsteady base flow is saved every 100 time steps, corresponding to time interval $\Delta T = \Delta t \times 100 = 0.5$, which was found to be adequate for both the individual vortex and co-rotating vortex pair cases at the highest Reynolds number considered, $Re = 3000$, on the basis that the relative change of maximum transient energy growth fell below 0.2 % when using $\Delta T = 0.3$.

5. Linear transient energy growth

Three representative cases are considered in what follows. In each, the dynamics of a co-rotating vortex pair and that of an individual vortex are compared. In the first case for $q = 0.8$, the individual vortices have a strong inviscid-type helical instability and the amount of transient energy growth exhibited by the pair is very similar to that for an individual vortex out to the time-horizon considered, which precedes merging. This similarity reflects the fact that the transient growth mechanism for each vortex

https://doi.org/10.1017/jfm.2012.171 Published online by Cambridge University Press

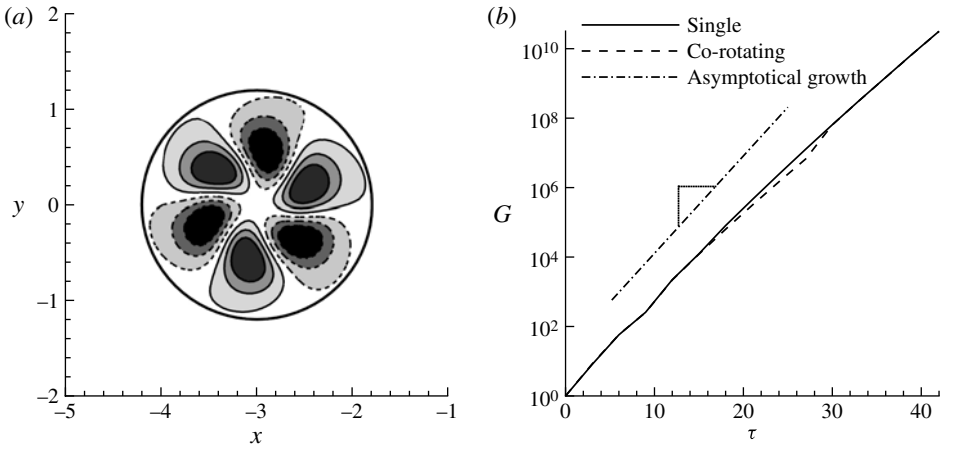


FIGURE 4. Inviscidly unstable helical eigenmode (a), for an individual vortex at $(Re, q, k) = (1000, 0.8, 1.7)$; dashed/solid lines denote positive/negative axial vorticity; thick solid line is the contour line of axial vorticity 1.5 in the base flow. A comparison of transient energy growth for the individual vortex and for a vortex pair composed of unstable individual vortices is shown in (b). The growth rate of the helical instability is $\sigma = 0.323$ and the corresponding energy growth rate is 2σ, as illustrated by the slope of the dash-dotted line in (b), see the text.

of the pair is substantively the same as for an isolated vortex. In the second case for $q = 2$, the individual vortices have a weak viscous-type core instability, transient energy growth for the pair is somewhat larger than for an individual vortex, and the mechanism for transient growth in the pair is rather different to that of an individual vortex. In the third case for $q = 3$, the individual vortices are asymptotically stable but exhibit moderately strong transient growth; transient growth is substantially larger for the pair, and as we will show in § 6, can influence the time taken for vortex merging.

5.1. *Inviscidly unstable vortices; $q = 0.8$, $Re = 1000$*

First we focus on the influence of the strain field imposed by an adjacent vortex on the most unstable mode of an individual vortex, i.e. the widely investigated helical unstable mode, in a co-rotating vortex system. We also take into account the rotation effect of the vortex pair by using a time-dependent base flow. The adoption of non-periodic unsteady base flow excludes the calculation of asymptotic instabilities but if the most unstable mode associated with the time-frozen base flow is dominant, the optimal perturbation is expected to have a similar structure with this least stable mode. Therefore, the flow parameters are set to $(Re, q, k) = (1000, 0.8, 1.7)$ in order to activate the inviscid helical instability of the individual vortex, with the corresponding eigenmode illustrated in figure 4(a). The axial wavenumber $k = 1.7$ is adopted to maximize the asymptotic growth rate at these values of Reynolds number and swirl strength for an individual vortex (Broadhurst 2007). The merging threshold of the base flow is not reached in the time interval considered. From the transient optimal growth envelopes illustrated in figure 4(b), it can be inferred that normal/eigenmodal instabilities dominate in both the individual vortex and the vortex pair and there are limited non-normal transient effects over small time intervals. The energy growth of the co-rotating vortex pair is slightly smaller than that of the individual vortex (the difference is negligible compared with the magnitude of G at $\tau > 30$), due to the

https://doi.org/10.1017/jfm.2012.171 Published online by Cambridge University Press

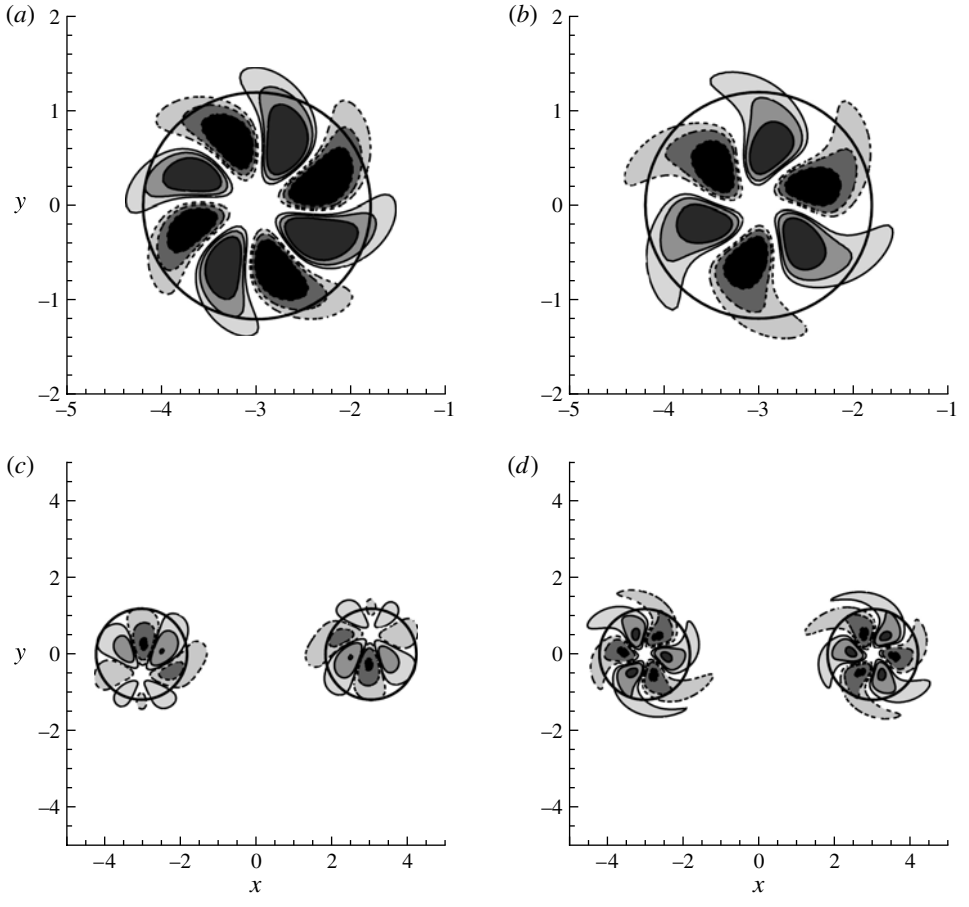


FIGURE 5. Contours of axial vorticity for optimal initial perturbations of an individual vortex and (*a*) $\tau = 3$, (*b*) $\tau = 27$, and a pair of co-rotating vortices at (*c*) $\tau = 3$, (*d*) $\tau = 27$, when the individual vortex is inviscidly unstable at $(Re, q, k) = (1000, 0.8, 1.7)$. Dashed/solid contour lines denote positive/negative vorticity and the thick solid line is the contour line of axial vorticity 1.5 in the base flow.

interaction between vortices over large time intervals. As may be seen, the large time-horizon rate of increase of G with τ for both the individual vortex and the vortex pair is smaller than (twice) the growth rate of the helical unstable mode, for which $\sigma = 0.323$. This difference is accounted for by the fact that the base flows used in the transient growth studies decay over time, whereas in the calculation of σ, the base flow is considered time independent.

The optimal perturbations and outcomes are summarized in figure 5. For the individual vortex, the optimal perturbation at small τ has four pairs of helical structures, but for larger τ the optimal perturbation takes on the threefold symmetry of the eigenmode, as shown in figure 4(*a*). This mode transfer occurs because at small time intervals, when the non-normal effects are evident, the growth with $m = 4$ is larger than that with $m = 3$, while at large time horizons, when the non-normal effects vanish and the asymptotic instabilities become dominant, the growth with $m = 3$ is larger than that with $m = 4$ (at the parameters investigated, the largest energy growth

https://doi.org/10.1017/jfm.2012.171 Published online by Cambridge University Press

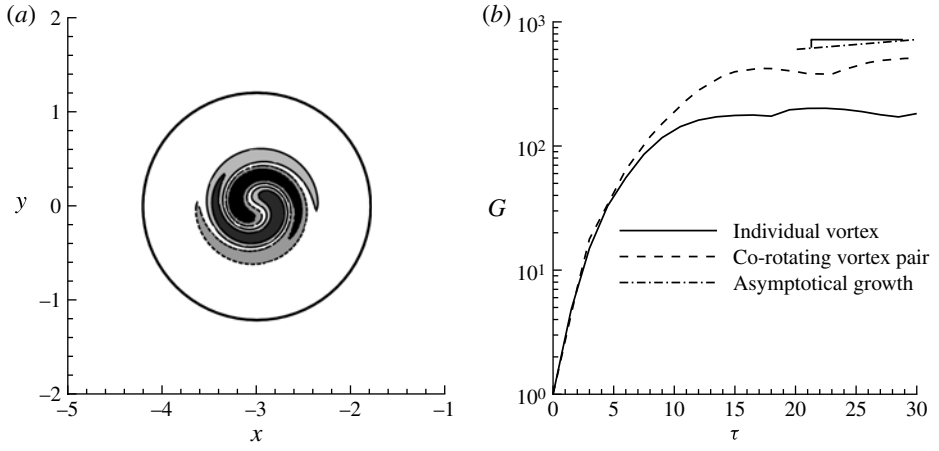


FIGURE 6. Contours of axial vorticity of the asymptotic instability of an individual vortex (a) and transient energy growth of the individual vortex and a vortex pair composing of viscously unstable individual vortices (b) at $(Re, q, k) = (3000, 2, 0.27)$. In the contour plot, dashed/solid lines denote negative/positive vorticity and the thick solid line is the contour line of axial vorticity 1.5 in the base flow. The growth rate of the helical instability is $\sigma = 9.17 \times 10^{-3}$ and the corresponding eigenmodal energy growth rate is 2σ, as illustrated by the slope of the dash-dotted line in (b).

rate of asymptotic instabilities is obtained at $m = 3$, see Broadhurst 2007). For the vortex pair, the optimal perturbation for $\tau = 3$ consists of two separated structures located in the vortex cores and, as for the optimal perturbation for an individual vortex of this type and for the same time horizon, each core structure has four pairs of spiral arms. However, these pairs lack strict fourfold symmetry, although the perturbations within each core more closely approach this as time evolves. It is notable that the overall structure of the perturbation for the pair system has a 180° rotation symmetry with respect to the centroid of the base flow $(x, y = 0, 0)$. For $\tau = 27$, as mentioned previously the optimal structure in each core takes on the threefold structure possessed by both the single-vortex eigenmode and the optimal perturbation in an individual vortex for longer time horizons. However, again the initial perturbation in each core lacks complete rotation symmetry; each helical mode consists of three spiral arms with two pairs stronger than the remaining one. There is also a slight elliptic deformation of the structure, with the axes of the ellipse tilting from the x- and y-axes owing to the rotation of the base flow. This mode can be interpreted as an elliptically deformed helical instability which is the resonant interaction between the strain field and Kelvin waves with azimuthal wavenumbers $m = -3$ and $m = -1$, as reported by Lacaze *et al.* (2007) and Roy *et al.* (2008) in their asymptotical stability studies with counter-rotating and co-rotating vortex pairs, respectively. Once again it appears that there is a 180° rotation symmetry of the complete structure about the centroid of the base flow.

5.2. *Viscously unstable vortices: $q = 2$, $Re = 3000$*

At parameter values $(Re, q) = (3000, 2)$, individual Batchelor vortices exhibit viscous-type instability, with spiral eigenmodal structure confined mainly to the viscous core region, as illustrated in figure 6(a); the concentration of perturbation energy around the vortex axis has led to these instabilities often being referred to as centre modes.

https://doi.org/10.1017/jfm.2012.171 Published online by Cambridge University Press

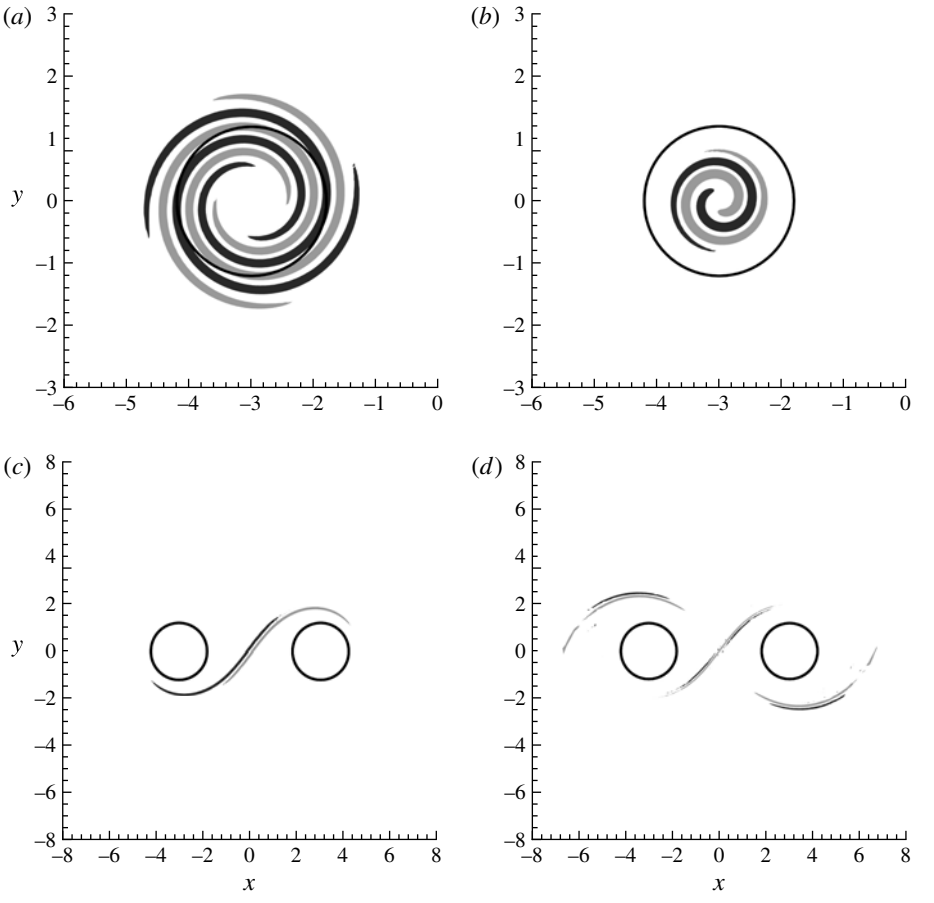


FIGURE 7. Axial vorticity contours of optimal initial perturbations of an individual vortex (*a,b*) with $\tau = 9$, 30, and a pair of co-rotating vortices (*c,d*) with $\tau = 9$, 30, when the individual vortex has viscous centre instability at $(Re, q, k) = (3000, 2, 0.27)$. Two contour levels are used and contour lines are removed for clarification. Dark shading represents positive vorticity, light shading represents negative vorticity, and the thick solid line is the contour line of axial vorticity 1.5 in the base flow.

The axial wavenumber is set to $k = 0.27$ in order to activate the most unstable mode for an individual vortex for the parameters considered and investigate the effects of strain field on the well-documented viscous centre mode. Although in this case the vortices are individually asymptotically unstable, the growth rate is relatively slow when compared with the transient growth for $\tau < 10$. So in comparison to the $q = 0.8$ study we observe a strong initial growth due to non-normal transients.

Transient energy growth for an individual vortex and a vortex pair when viscous centre instability appears is shown in figure 6(*b*). In each case the envelope curve consists of several segments due to jumps in symmetry properties of the optimal perturbation with increasing τ, as also happens in the inviscidly unstable case discussed in the previous section. For example, from the optimal perturbations of the individual vortex in figure 7(*a,b*), we note that for $\tau = 9$, there are two pairs of spiral branches in the optimal structure but at $\tau = 30$, the number has reduced to

https://doi.org/10.1017/jfm.2012.171 Published online by Cambridge University Press

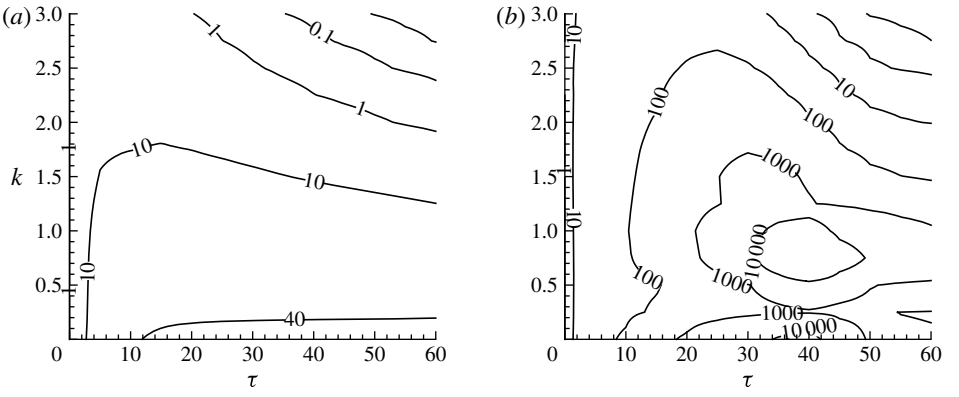


FIGURE 8. Contours of optimal energy growth G_{max} as a function of time horizon τ and axial wavenumber k for (*a*) an individual vortex and (*b*) a co-rotating vortex pair. In (*b*), there are two local maxima, the first for ($k = 0$, $\tau = 39$), where $G_{max} = 1.45 \times 10^4$, and the second for ($k = 0.75$, $\tau = 40$), for which $G_{max} = 4.56 \times 10^4$. The cases considered employed a swirl strength where individual vortices are asymptotically stable ($Re = 100$, $q = 3$).

one, and the optimal initial perturbation resembles the adjoint of the leading unstable viscous centre mode.

The optimal initial perturbation structure of the vortex pair at $\tau = 9$ (figure 7*c*) lies predominantly in the interaction region between the vortex cores. At $\tau = 30$ (figure 7*d*) there are perturbations associated with each individual vortex, and these are of similar magnitude to the interaction-region structure. This structural change is reflected in the segmented rise of energy growth with τ corresponding envelope curve shown in figure 6(*b*). The expansion of the potential region structure with τ is a reflection of the optimal perturbation in the individual vortex whose radius expands with increasing τ. We note that the optimal initial perturbations for the pairs are different to those for an individual vortex in the sense that those for the individual vortex lie within the core (directly exciting eigenmodal structure) while those for the pairs lie outside the cores, in the regions which can be initially considered as potential flow. With increasing time however, perturbations to the pairs progress to the core regions, in a manner similar to the observations made for stable vortex pairs (as will be discussed in § 5.3). This type of growth is analogous to the resonance effect first proposed by Antkowiak & Brancher (2004). This transformation of energy from the potential-flow region to the vortex core owes to the non-normality of the potential eigenmodes, which are either in the form of one wave packet outside the vortex core or of two wave packets, with one inside the core and the other outside it (Mao 2010).

5.3. *Asymptotically stable vortices: $q = 3$, $Re = 100$*

In this final case we investigate transient growth within the co-rotating vortex pair composed of vortices with $Re = 100$ and $q = 3$, which individually are asymptotically stable at all axial wavenumbers (Fabre & Jacquin 2004). Significant transient growth for an individual vortex with $q = 3$ (but at a larger Reynolds number) was reported by Heaton (2007*a*). Contours of optimal energy growth G_{max} with time horizon τ and wavenumber k as independent variables are shown in figure 8 for both individual vortices and vortex pairs. Over the time horizons considered, $\tau = 0$–60, maximum transient energy growth for the vortex pair is two to three orders of magnitude

https://doi.org/10.1017/jfm.2012.171 Published online by Cambridge University Press

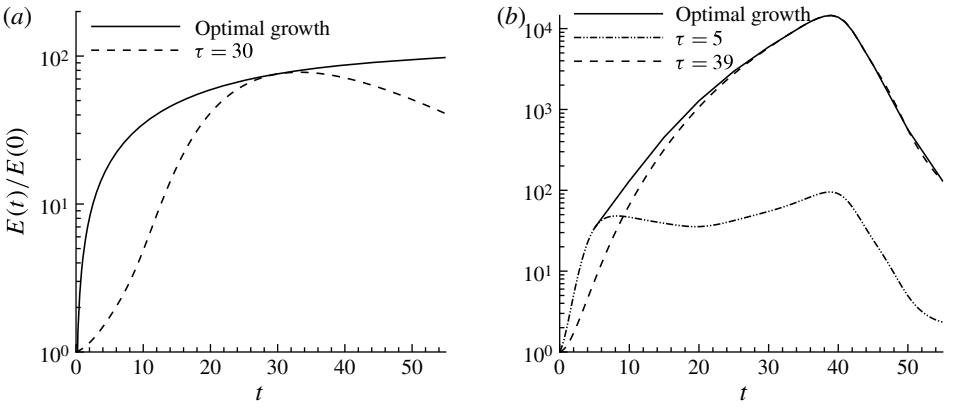


FIGURE 9. Optimal energy growth envelopes (solid lines) and representative transient responses (dashed/chained lines) for two-dimensional perturbations to stable vortices (with $q = 3$, $Re = 100$): (a) growth for an individual vortex and (b) growth for a co-rotating vortex pair.

larger than that for the individual vortex. For individual vortices, maximum transient energy growth occurs for axially invariant flows, i.e. $k = 0$, while the distribution of G_{max} for pairs is bi-modal, with maxima occurring both for ($k = 0$, $\tau = 39$), where $G_{max} = 1.45 \times 10^4$, and for ($k = 0.75$, $\tau = 40$), for which $G_{max} = 4.56 \times 10^4$. The bi-modal behaviour for pairs is associated with two distinct physical mechanisms, as we will show in what follows.

In the remainder of this section, we first examine the details of behaviour for two-dimensional perturbations ($k = 0$) owing to its simplicity and comparatively large transient growth. Then we examine behaviour for axial wavenumber $k = 0.75$, which gives the maximum transient growth. We note that there are significant differences between the linear/nonlinear behaviours of these two cases, as will be further examined in § 6.

5.3.1. *Two-dimensional perturbations, $k = 0$*

Figure 9 shows the optimal growth and transient responses of the individual vortex and the co-rotating vortex pair for perturbations with axial wavenumber $k = 0$. The optimal growth curve can be understood as the envelope of the individual responses evolved from optimal perturbations corresponding to different time horizons τ, as indicated in the plot. From the energy growth curve of the individual vortex (see figure 9a), we see that there is reasonably strong transient growth before $\tau = 10$ and then the growth increases more slowly. A large time interval is therefore required to reach the maximum growth of the individual vortex (in agreement with Heaton & Peake 2007). Because our focus is concerned with the dynamics of vortex pairs rather than those for an individual vortex, we have not extended the range of τ to find the maximum energy growth of an individual vortex.

In the transient growth plot of the vortex pair illustrated in figure 9(b), we note that the maximum growth in the co-rotating vortex pair occurs for $\tau = 39$, which corresponds to the vortex merging phase in the base flow shown in figure 3(c). Two individual optimal growth profiles are also shown, for $\tau = 5$ and $\tau = 39$. There is however another local maximum of transient growth for the $\tau = 5$ initial perturbation

https://doi.org/10.1017/jfm.2012.171 Published online by Cambridge University Press

near $t = 5$, which is induced by transient effects of the individual vortices rather than vortex interaction.

Contours of axial vorticity of the optimal initial perturbations and outcomes are illustrated in figure 10. The optimal initial perturbation of the individual vortex is concentrated in the potential-flow region and moves away from the vortex core as τ increases. This structure can be interpreted as a combination of potential eigenmodes, whose energy is concentrated in the potential region in both the Lamb–Oseen vortex (Fabre, Sipp & Jacquin 2006) and the Batchelor vortex (Mao 2010). From the outcome of the optimal initial perturbation at $t = \tau = 30$, we see that the energy inside the vortex core becomes dominant and the structures in the potential-flow region are negligible. This transient growth mechanism has been described as a combination of Orr and induction effects associated with a vortex core contamination in the context of a Lamb–Oseen vortex (Antkowiak & Brancher 2004). In their work Antkowiak & Brancher argue that the unwinding, under a Orr-type motion, of the spiral structure in the axial vorticity perturbation shown in figure 10(*a*) leads to a radial velocity in the core regions. Consideration of the linearized vorticity equations then highlights how the presence of a radial perturbation velocity permits the base flow axial vorticity to be induced into the core perturbation region as shown in figure 10(*b*).

The evolution of the $\tau = 5$ and the $\tau = 39$ initial perturbation to the co-rotating vortex pair is similar to that of the perturbation in the individual vortex over short time intervals ($t < 10$) before the merging phase. Therefore, the initial conditions shown in figure 10(*c,d*) undergo an initial Orr-type unwrapping leading to a radial velocity that induces axial vorticity in the core regions. The initial structure is concentrated in the potential region of each vortex and in the interaction region around the centroid, where the strain rate will be maximized as the vortex system rotates. Careful consideration of the initial perturbation shown in figure 10(*c*) highlights that there is a rotational anti-symmetry about the centroid. As the perturbation evolves into the core region at $t = 5$ as shown in figure 10(*d*) the rotational anti-symmetry is maintained, however the secondary growth of this initial condition at $t = 39$ (see figure 9*b*) is associated with a perturbation which has a rotational symmetry broadly similar to that shown in figure 10(*f*). However, from the transient growth analysis at $\tau = 5$ there is a sub-dominant initial condition which has rotational symmetry and $\sim$10 % less growth at $t = 5$. This initial condition still evolves to a rotational symmetric state at $t = 39$ similar to figure 10(*f*). We next consider the optimal initial perturbation for $\tau = 39$ shown in figure 10(*f*) and note that the structure is rather different for $\tau = 5$. The structure of initial perturbation vorticity now has expanding spiral arms in the periphery of the circular region of rotation of the vortex pair, while the amount of perturbation in the interaction region is comparatively low. This initial condition is also rotationally symmetric. As time evolves, the Orr and induction effects drive the structure from being energetic in the potential zone to being energetic in the vortex cores. However, for this initial perturbation the solution at $t = 5$ maintains its rotational symmetry and we subsequently observe continued growth over the whole time interval up to $t \approx 39$. The rotational symmetry is consistent with the underlying symmetry of the merging base flow as discussed in Meunier *et al.* (2005). Inspecting the interaction of this perturbation with the base flow, we see that this perturbation at $t = \tau = 39$ displaces the vortex cores in the base flow and pushes the vortices towards each other, as illustrated in figure 10(*f*), where the solid arrows point to the rotation direction of the co-rotating vortices without being perturbed and the hollow arrows denote the moving direction of the base flow vortices after considering the displacement effects of the perturbations. Correspondingly if reversing the perturbation,

https://doi.org/10.1017/jfm.2012.171 Published online by Cambridge University Press

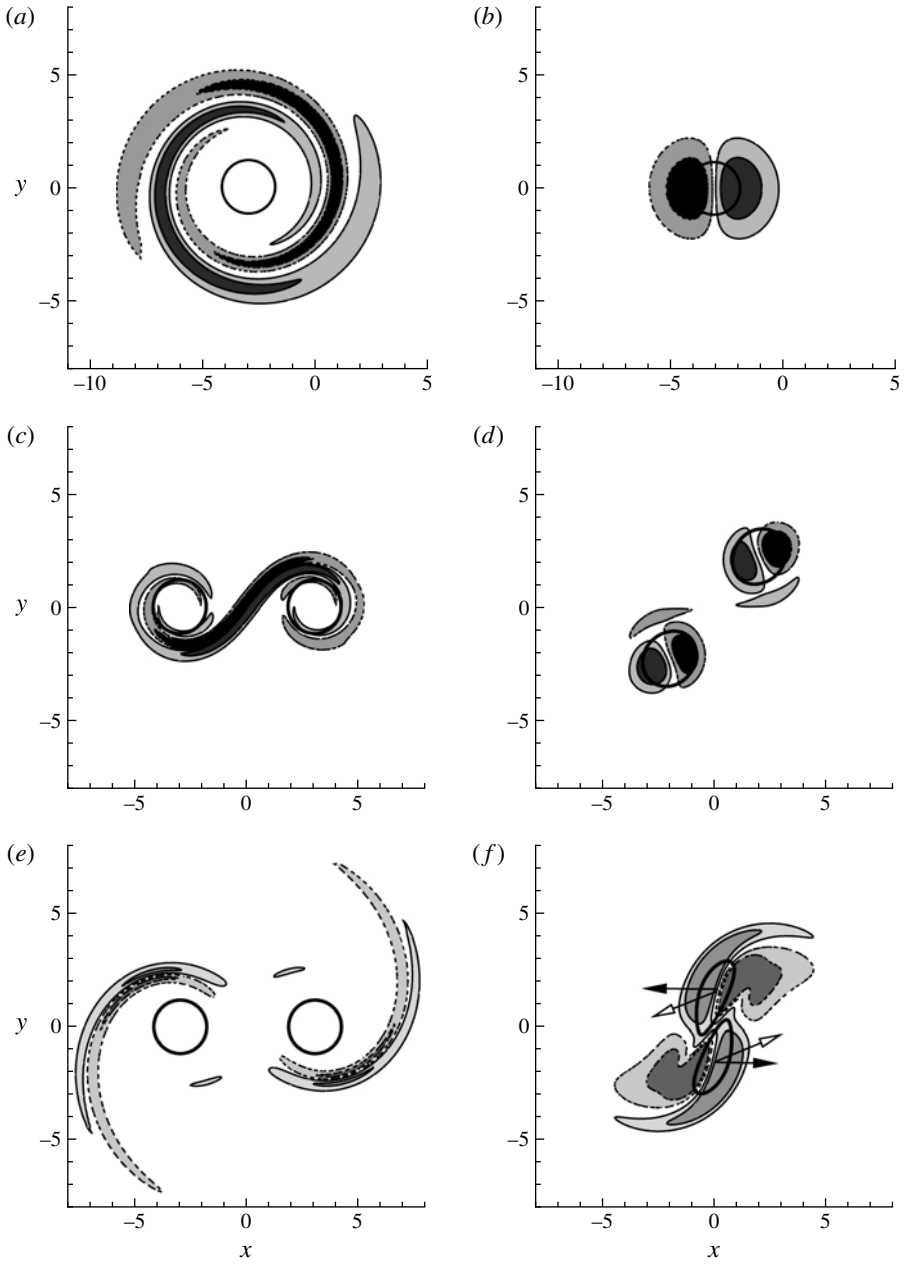


FIGURE 10. Contours of axial vorticity in optimal two-dimensional initial perturbations and outcomes for an individual vortex and a co-rotating vortex pair at $(Re, q, k) = (100, 3, 0)$. The initial and outcome perturbations are normalized to have the same energy. Dashed/solid lines denote negative/positive vorticity and the thick solid line is the contour line of axial vorticity 1.5 in the base flow. (*a,b*) initial perturbation and outcome for an individual vortex, with time horizon $\tau = 30$, energy growth $G = 75.7$. (*c,d*) initial perturbation and outcome for a vortex pair, with time horizon $\tau = 5$, energy growth $G = 32.0$. (*e,f*) initial perturbation and outcome for an vortex pair, with time horizon $\tau = 39$, energy growth $G = 1.45 \times 10^4$. The filled arrow in (*f*) denotes the moving direction of the vortices in the base flow without being perturbed and the hollow arrows denote the displacement direction of the perturbation on the vortices in the base flow.

https://doi.org/10.1017/jfm.2012.171 Published online by Cambridge University Press

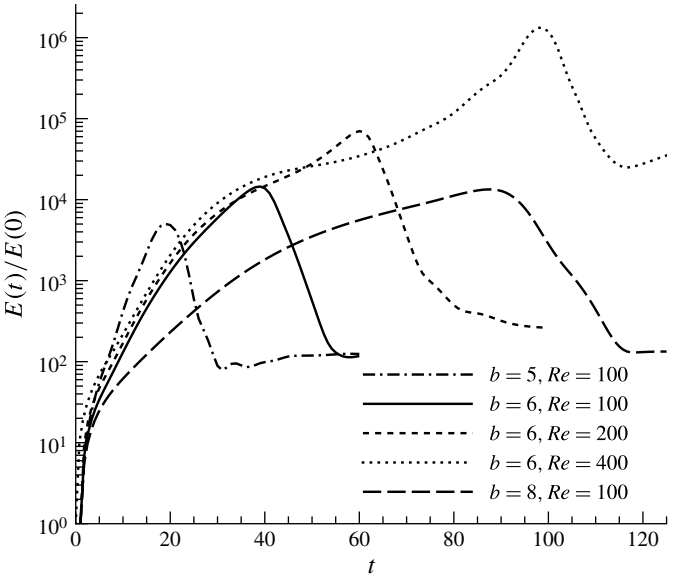


FIGURE 11. Transient growth envelopes at various initial Reynolds numbers and initial core spacings, with $(q, k) = (3, 0)$.

the displacement effect turns to pull the vortices away from each other. Therefore, it can be expected that this perturbation has the potential to control (delay or accelerate) the merging process of the base flow. This control effect will be verified in § 6.1.

One may argue that the significant rise of optimal energy growth around the merging phase is due to the larger swirl number of the single vortex formed after merging, but the optimal energy growth of the Batchelor vortex at $q = 6$, which is twice as strong in swirl than the vortex studied here, is $G = 198.2$ at $\tau = 39$, so the increase of swirl strength is not the principal reason for the large transient growth close to the merging point. In addition, when the base flow merges, the perturbations in the cores of the pair of vortices are in opposite phases so they cannot merge to form a perturbation in the core of the combined vortex, as shown in figure 10(*f*).

Transient growth during the merging process at other values of vortex distance and Reynolds numbers has also been examined, as illustrated in figure 11. We note that a longer time interval is required to obtain merger at larger values of either b or Re. In all of the cases examined, the transient growth rises rapidly before the merging phase and reflects the transient dynamics of an individual vortex after merging into a single vortex. Therefore, the parameters we initially considered ($b = 6$ and $Re = 100$) incorporate the typical transient dynamics of a co-rotating vortex pair (at least in the range of Reynolds numbers considered), and produces vortex merging over a reasonably small time interval.

5.3.2. *Three-dimensional perturbations at axial wavenumber* $k = 0.75$

Having examined axially homogeneous perturbations, we now turn our attention to the optimal perturbations for $k = 0.75$, which at a time horizon of $\tau = 40$ provides the global maximum transient energy growth for the pair system in figure 8. Figure 12 illustrates optimal energy growth profiles (solid lines) and representative transient responses (dashed lines) of global optimal perturbations when $\tau = 40$. We note that for

https://doi.org/10.1017/jfm.2012.171 Published online by Cambridge University Press

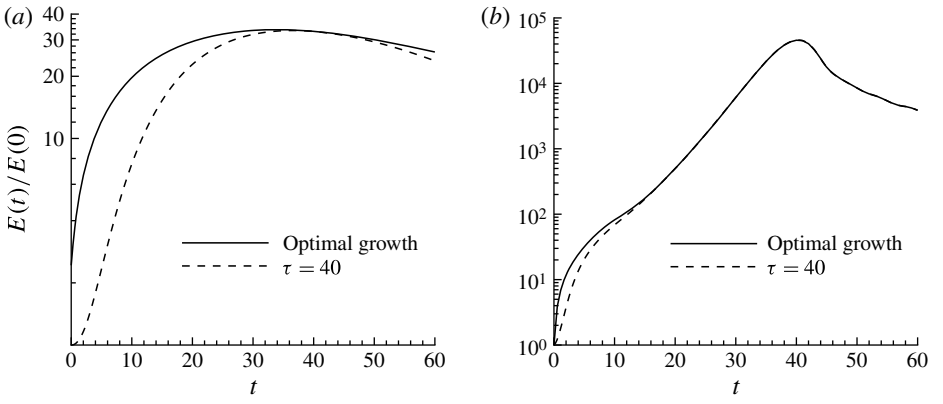


FIGURE 12. Optimal energy growth envelopes (solid lines) and representative transient responses (dashed lines) for perturbations to stable vortices with $(Re, q, k) = (100, 3, 0.75)$: (*a*) growth for an individual vortex and (*b*) growth for a co-rotating vortex pair.

the co-rotating vortex pair, the transient energy growth indicated by the dotted line is slightly smaller than the optimal growth envelope when $t < 20$, while the two curves almost overlap at greater times. Once again the co-rotating vortex pair transient growth is two to three orders of magnitude larger than for the isolated vortex. Similar to the optimal growth envelopes of the two-dimensional problem the envelopes for both the isolated vortex and for the co-rotating vortex pair have similar magnitudes for $\tau < 10$. For larger values of τ, however, we again for the pair observe a significant growth up to the merging phase at $\tau \approx 40$ where the growth is of order 10^4.

In attempting to explain why we observe such significantly higher growth in the vortex pair case, we consider in figure 13 the spatial structures of the optimal initial perturbations, and the outcomes obtained by linear evolution at intermediate and maximal-growth times. In figure 13(*a*) we show the two-dimensional Fourier coefficient of the initial optimal perturbation of the isolated vortex which if plotted as a three-dimensional iso-contour correlates very well with the Lamb–Oseen case investigated by Antkowiak & Brancher (2004, figure 2). Antkowiak & Brancher conjecture that the transient growth of the isolated vortex is a resonance phenomenon, as is also supported by the results of Pradeep & Hussain (2006). The resonance was related to an interaction between the outer potential mode and an inner discrete Kelvin-type mode. It would seem likely that the earlier growth for $\tau < 10$ in the co-rotating vortex pair results from a similar phenomenon.

The optimal initial disturbance for the co-rotating pair is shown in figure 13(*c*) and similar to the initial perturbation of the two-dimensional case shown in figure 10 we observe an energetic initial perturbation in the outer potential region around the base flow cores. In this case we have a similar level of perturbation in both the interaction region between the vortex cores and in the spiralling region at the outer part of the cores. We note that this initial perturbation is rotationally asymmetric. The significant additional transient growth for $\tau > 10$ shown in figure 12 still requires explanation. The obvious candidate for physical mechanism underlying transient growth in this three-dimensional case is elliptic instability, but any precise analysis is clouded by the fact that quasi-steady assumptions cannot be made, since core sizes and spacing vary rapidly in time during the merging process. Examination of contours of axial vorticity associated with the optimal perturbation for $\tau = 40$ at intermediate times, as plotted in

https://doi.org/10.1017/jfm.2012.171 Published online by Cambridge University Press

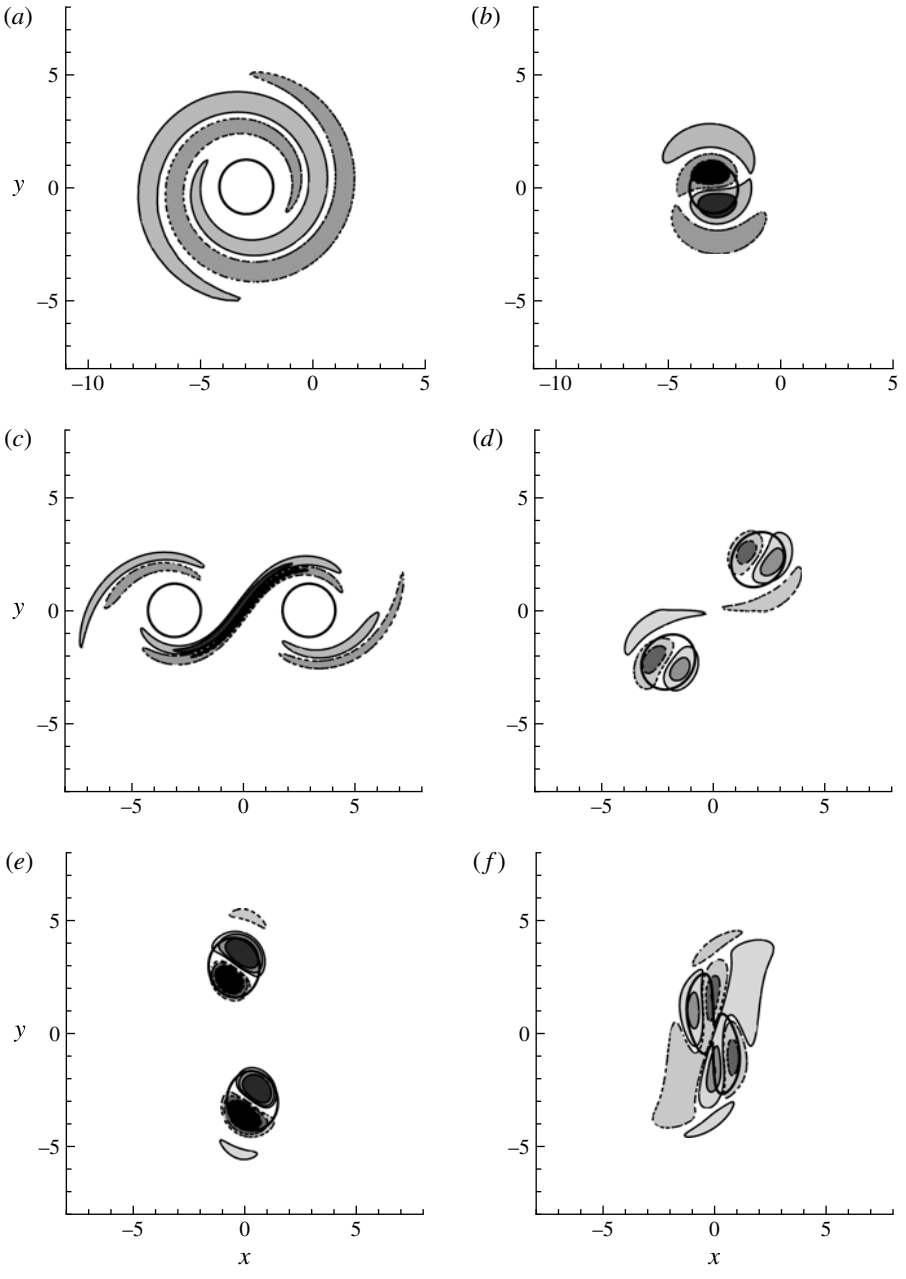


FIGURE 13. Contours of axial vorticity in optimal three-dimensional perturbations and outcomes in an individual vortex and a co-rotating vortex pair for axial Fourier modes at $(Re, q, k) = (100, 3, 0.75)$, where the flow is stable. Initial and outcome perturbations are normalized to the same energy. (*a,b*) Initial perturbation and outcome for an individual vortex, time horizon $\tau = 40$ and energy growth $G = 26.1$. (*c–f*) Development of perturbations for a vortex pair at $t = 0, 5, 10, 40$ respectively, time horizon $\tau = 40$ and energy growth $G(\tau) = 4.56 \times 10^4$. Dashed/solid lines denote negative/positive vorticity and the thick solid line is the contour line of axial vorticity 1.5 in the base flow. For the computation at $\tau = 40$, the mesh outside the vortex core was slightly refined.

https://doi.org/10.1017/jfm.2012.171 Published online by Cambridge University Press

figure 13 at $t = 5$, 10, shows structure comparable with $m = 1, -1$ asymptotic modes obtained by quasi-steady analysis by Roy *et al.* (2008, see figure 3 of that paper). We therefore conjecture that the co-rotating vortex pair considered undergoes growth due to an elliptic-type instability between $10 < t < 40$ before the rapid variation of the base flow at merging brings this to an end, causing growth to saturate and eventually decay.

6. DNS of linearly stable vortex pairs with optimal perturbations

Nonlinear evolution of optimal perturbations to co-rotating vortex pairs obtained in asymptotically stable cases at $(Re, q) = (100, 3)$ and with $k = 0$ and $k = 0.75$ is investigated to highlight the physical performance of the optimal perturbations which display large linear energy growth. Nonlinear behaviour of optimal perturbations in the inviscidly unstable and viscously unstable cases is not examined, since for the inviscid case, linear dynamics are dominant and strong, while for the viscously unstable case, both non-normal and linear growth are weak.

6.1. *Two-dimensional DNS at* $k = 0$

In the axially homogeneous case, $k = 0$, we first examine the effect of introducing the optimal perturbation at a small relative energy level but where the sign of the perturbation is changed. In the linear case such a change of sign has no effect on transient energy growth since the perturbation is an eigenmode of the operator $\mathscr{A}(\tau)\mathscr{A}^*(\tau)$. However, in the nonlinear system we find that changing the sign of the optimal initial perturbation has a significant effect, which is to either promote or delay vortex merging. We choose to define a positive-signed perturbation as one that pushes the two vortices in base flow towards each other and correspondingly a negative-signed perturbation as one that pulls the vortices in base flow away from each.

Initially, the optimal linear perturbation is added to the base flow at relative energy level $\pm 1 \times 10^{-4}$, and the perturbed flow is evolved through DNS to a final time horizon. Two typical optimal perturbations, obtained at $\tau = 5$ and $\tau = 39$ respectively, are used as the initial disturbances. Vorticity contours for the initial perturbed flow and resulting evolutions are shown in figure 14. These may be compared with the equivalent unperturbed cases shown in figure 3(*c,d*). For time horizon $\tau = 5$, well before vortex merging occurs, the dynamics reflects the transient characters based on the quasi-stationary base flow of the co-rotating vortex system. The perturbed outcomes for $t = \tau = 5$ are shown in figure 14(*a,c*). The initial perturbation, which for this time horizon is strongest in the interaction region, see figure 10(*c*), does not influence the dynamics of the vortex system significantly, regardless of sign. However, for time horizon $\tau = 39$ corresponding to vortex merger in the unperturbed case, we find that changing the sign of perturbation substantively alters outcomes, as may be seen by examining figure 14(*b,d*) and comparing these with figure 3(*d*). Clearly, perturbation of a positive sign induces the pair to merge more rapidly, whereas the reverse is true for the negative perturbation.

In the outcome of the optimal perturbation as shown in figure 10(*f*), we see that the superposition of perturbation and base flow generates displacement effects on the vortices in the base flow and changes the rotation direction of the vortices. Mao & Sherwin (2012) have observed this optimal-perturbation-induced displacement of the vortex core in the context of an individual vortex, which is referred to as 'vortex meandering'. The displacement effect here can be considered as a synchronized dual vortex meandering, where the two vortices are displaced in such a direction to be closer to each another and accelerate the vortex merging. Clearly if reversing the

https://doi.org/10.1017/jfm.2012.171 Published online by Cambridge University Press

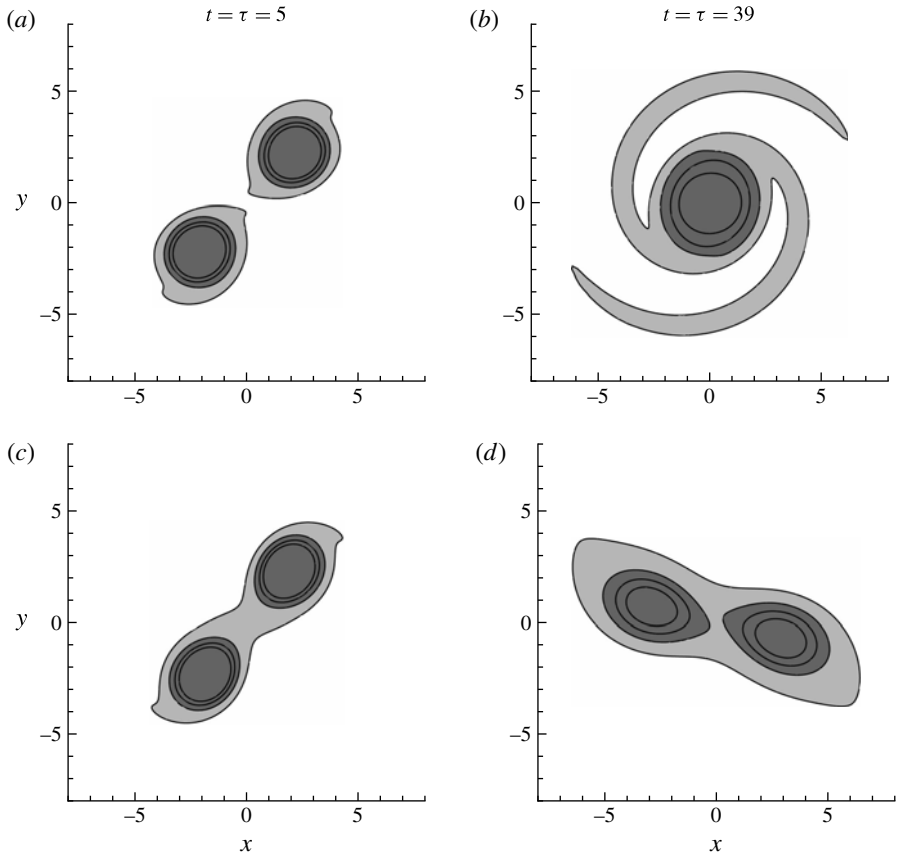


FIGURE 14. Axial vorticity contours for two-dimensional DNS of vortex pairs at $(Re, q, k) = (100, 3, 0)$, showing the effect of either positive of negative perturbations. Compare with the equivalent unperturbed results shown in figure 3(*b,c*), which share contour levels with the present figure: (*a,b*) relative perturbation level $+1 \times 10^{-4}$ at $t = \tau = 5$ and $t = \tau = 39$, and (*c,d*) -1×10^{-4} at the same instants; see the text for the discussion of signs.

direction of the initial perturbation, the base flow vortices will be pulled away from each other and subsequently merge at a later time.

Our next consideration is the nonlinear effect of the relative amplitude of two-dimensional perturbations. Figure 15(*a*) illustrates the saturation of perturbations at increasing initial relative energy level in the nonlinear evolution compared with the linear optimal growth. The energy of perturbations for nonlinear evolution is obtained by integrating over the domain after subtracting the base flow field from the outcomes of nonlinear evolution. The first effect to be observed is that increasing initial perturbation magnitude leads to reduced energy growth and saturation at earlier times, compared with the linear case; similar nonlinear outcomes have been observed in other flows (e.g. Blackburn *et al.* 2008). The effect of perturbation sign on saturation amplitude is not particularly strong, however negative perturbations delay saturation compared with positive perturbations; this delay can be associated with delayed vortex merging.

Figure 15(*b*) shows more directly the nonlinear effect of perturbation on vortex merging, as assessed from vortex core distance, being the distance between the

https://doi.org/10.1017/jfm.2012.171 Published online by Cambridge University Press

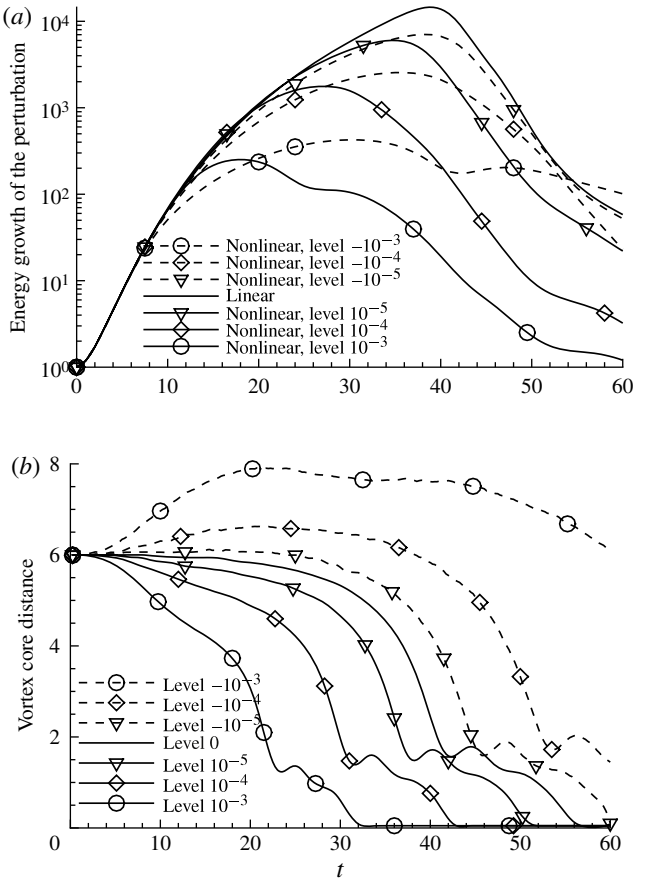


FIGURE 15. Examining the nonlinear effect of increasing perturbation level for $(Re, q, k) = (100, 3, 0)$: (*a*) energy growth, where in the nonlinear cases the energy in the perturbation is obtained after subtracting the unperturbed base flow; (*b*) vortex core distance.

centroids of the vortices where axial velocity and axial vorticity reach maxima. It may be seen that positive-signed perturbations of increasing size promote merger (reduce core distance more rapidly), while the reverse is true of negative-signed perturbations. In fact, negative perturbations can lead initially to an increase in vortex core distance, before merging inevitably occurs. It can also be observed that a comparatively small positive perturbation (relative energy level 1×10^{-3}) approximately halves the time required for vortex merging in this system. We note that for the unperturbed case of figure 15(*b*), the evolution of vortex core distance with time is similar to the final stages (2–4) of merging as seen in figure 5 of Meunier *et al.* (2005). This supports our supposition (see § 1) that our initial choices for Re and $a(0)/b$ are adequate to encompass the merging process.

If this axially homogeneous initial perturbation varies sinusoidally in the axial direction, then the vortex pair rotates with various speeds and the merging can be delayed, accelerated or unaffected at different axial locations. Therefore it can be anticipated that an initial perturbation with non-zero axial wavenumber has the potential to lead to breakup of the vortex pair. In the following section, we examine

https://doi.org/10.1017/jfm.2012.171 Published online by Cambridge University Press

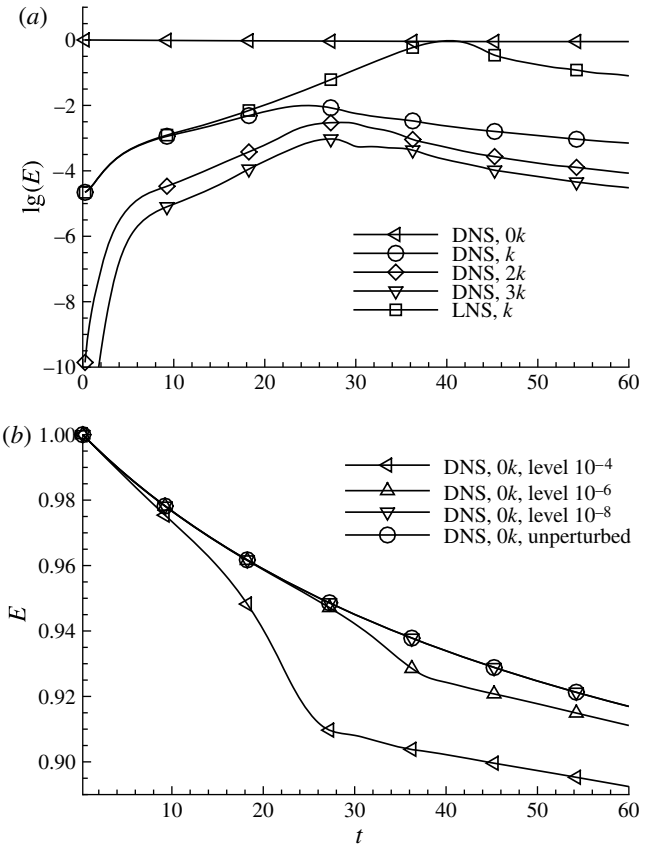


FIGURE 16. (*a*) Energy growth of perturbations at different axial modes in DNS and LNS, where $(Re, q, k) = (100, 3, 0.75)$. (*b*) Development of the axially invariant energy component in perturbed and unperturbed conditions with various initial perturbation energy levels. The values are normalized by the energy of the initially unperturbed flow.

the nonlinear evolution of the optimal initial perturbation at $k = 0.75$ and inspect effects of three-dimensional perturbation developments.

6.2. *Three-dimensional DNS with* $k = 0.75$

Nonlinear development of the optimal perturbation obtained at $k = 0.75$ is conducted by perturbing the initial base flow with the global optimal perturbation (for $\tau = 40$) at a relative energy levels 1×10^{-8}, 1×10^{-6} and 1×10^{-4}. (As noted in § 5.3.2, the sign of perturbation does not influence outcomes in the three-dimensional case, other than to shift the disturbance axially.) The axial extent of the computational domain is set to $L_z = 2\pi/k = 8\pi/3$ and Fourier expansions are used to discretize flows in the axial direction; 32 Fourier modes were used for the computations described below. The energy of the first five modes reported here has converged to three significant figures with respect to the number of axial Fourier modes.

Figure 16(*a*) shows the temporal evolution of energy in the first four axial Fourier modes with an initial perturbation of relative energy level 1×10^{-4} in the first non-zero mode (labelled mode k), and compares it to evolution of the same perturbation using LNS (with energy only in mode with axial wavenumber k), which is the same as

https://doi.org/10.1017/jfm.2012.171 Published online by Cambridge University Press

shown in figure 12(*b*). For clarity, energy evolutions in higher axial modes have not been plotted. For the DNS, energies in modes with axial wavenumber $2k$–$7k$ initially rise rapidly from zero as energy is redistributed nonlinearly from mode $k = 1$. As was the case in the two-dimensional DNS of § 6.1, nonlinear energy growth is lower than for the linear case, and saturation occurs earlier, at $t \approx 24$ compared with $t = \tau = 40$. The higher modes $(2k, 3k, \ldots)$ peak at slightly later times, and essentially are slaved to the fundamental mode. It may also be noted that up to $t \approx 10$, energy growth for mode k is much the same for both DNS and LNS.

Figure 16(*b*) illustrates the nonlinear effect of the optimal perturbation on energy in the axially averaged flow (i.e. in mode $0k$). We see that nonlinear effects induce significant reduction in axially averaged energy, especially at large perturbation levels. As expected, the energy history of the vortex with small initial perturbation level (1×10^{-8}) almost overlaps with that for the unperturbed vortex.

From the iso-surfaces of axial vorticity shown in figure 17, we see that at initial perturbation energy level 1×10^{-8}, the nonlinear development of the optimal perturbation has little influence on the merging process of the vortex pair, as illustrated in figure 17(*a*), but at larger perturbation levels 1×10^{-6} and 1×10^{-4}, nonlinear evolution of the optimal perturbations distorts the vortex pair and drives the vortices to break up before merging, as shown in figure 17(*b,c*). At the parameters considered in this case, the optimal transient growth in a single vortex is around three orders smaller than that in a vortex pair. For the largest initial perturbation level investigated, we did not observe vortex breakup in the context of a single vortex (see figure 17*d*) even though we note that Hussain, Pradeep & Stout (2011) had achieved a significant vortex core distortion by adopting large initial perturbations. Considering the range of initial perturbation energy adopted in this study, we do not attribute the break up with an isolated vortex mechanism. As already discussed in § 5.3.2 the co-rotating vortex pair undergoes significant transient growth in contrast to the isolated vortex and it seems plausible that this is due to an elliptic type instability. Indeed some suggestion of the elliptic nature of the instability is shown in middle image of figure 17(*c*) which is reminiscent of the images shown in Meunier *et al.* (2005, figure 11*b*) of the elliptic instability of two Kelvin waves of $m = 1$ and $m = -1$. Clearly in this case a two-dimensional vortex merging is not observed at large perturbation levels.

7. Discussion and conclusion

We have undertaken the transient growth analysis of a pair of identical Batchelor vortices, initially separated by a distance of six core radii, which was allowed to evolve until, in the unperturbed two-dimensional case, the vortices merge into a single structure. The evolution of the co-rotating vortex pair is analogous to the experimental results obtained by Meunier *et al.* (2005). Other separation distances were tested, from five to eight core radii, and the results were similar in terms of the forms of optimal structures obtained, and the shapes of the envelopes of energy growth up to the merging phase. Three representative cases have been investigated.

In § 5.1, the initial pair consisted of two vortices at $(Re, q) = (1000, 0.8)$ which are inviscidly unstable to helical modes when considered individually. Axial wavenumber $k = 1.7$ was investigated since at this wavenumber the asymptotical growth rate for an individual vortex reaches maxima. Over short time intervals, the optimal perturbation of the individual vortex have four pairs of spiral structures since this mode has the most rapid non-normal growth. However, for larger time horizon $\tau = 27$, the optimal structure converged to a double helical mode with each helical structure consisting

https://doi.org/10.1017/jfm.2012.171 Published online by Cambridge University Press

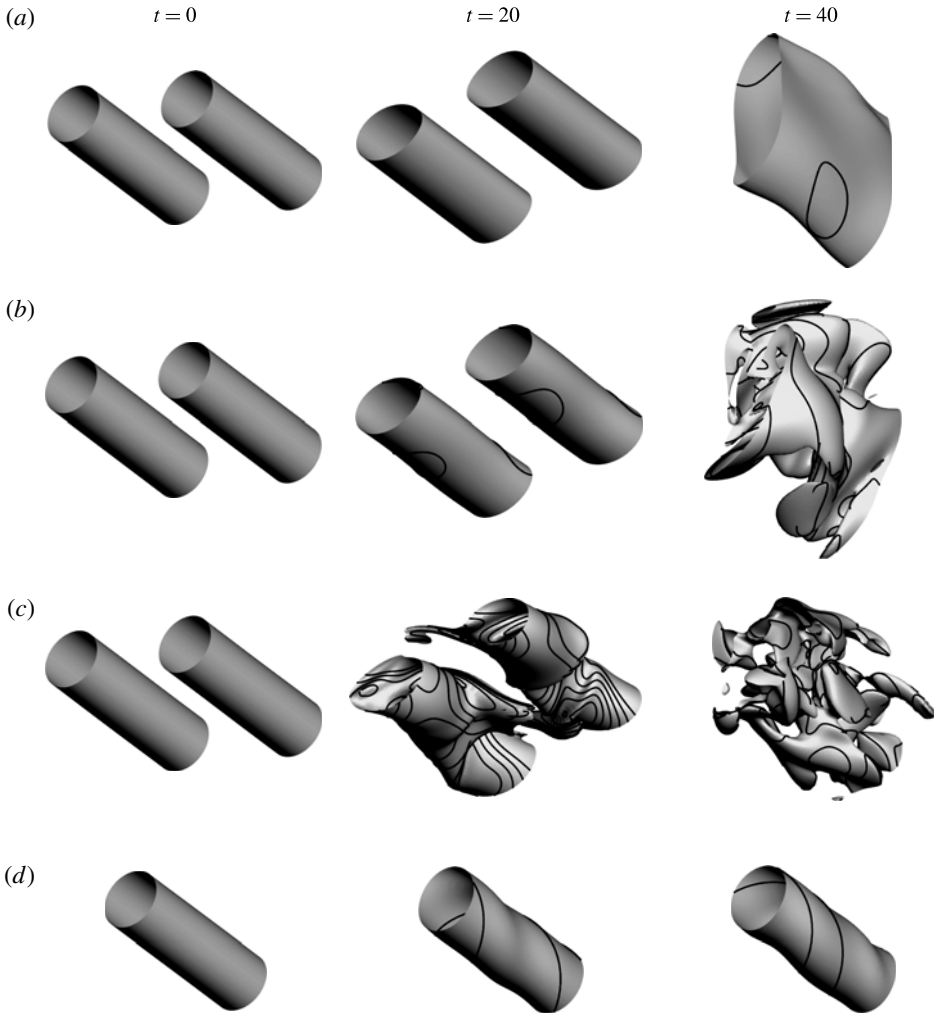


FIGURE 17. Iso-surfaces of axial vorticity $\zeta_z = 1$ in DNS at $(Re, q, k) = (100, 3, 0.75)$. The contour lines are associated with the axial velocity. Initial perturbation energy levels are (*a*) 1×10^{-8}, (*b*) 1×10^{-6}, (*c*) 1×10^{-4} for a vortex pair and (*d*) 1×10^{-4} for a single vortex.

of three pairs of vortices. Asymptotic instability analysis of the individual vortices demonstrate that the $m = 3$ modes have a larger growth than the $m = 4$ mode, which would suggest why this symmetry is selected at larger times.

In § 5.2, the pair consisted of two vortices at $(Re, q) = (3000, 2)$ is investigated and the streamwise wavenumber is set to $k = 0.27$ in order to maximize the individual viscous instabilities. The optimal structure of the initial perturbation of an isolated vortex at lower values of τ have four pairs of spiral structure which expand outside of the core region. However, for larger τ the isolated vortex optimal structure only contains one pair of spirals resembling more of the asymptotic instability. In contrast to the helically unstable case of $q = 0.8$ the optimal structure of the vortex pair is a combination of perturbations in the interaction region between the cores and circular regions outside of the base flow cores. At shorter time intervals the energy in the

https://doi.org/10.1017/jfm.2012.171 Published online by Cambridge University Press

interaction region dominates, but for larger optimal times ($\tau = 30$) the energy transfers more to the circular region in which the vortices rotate. For this case the transient growth of the co-rotating cortex pair is not significantly different in magnitude to the isolated vortex. The main significance of the non-normal transient growth is to provide a rapid growth up to $\tau < 10$ after which time the asymptotic instability starts to dominate.

In § 5.3, the base flow consisted of a pair of vortices for which $(Re, q) = (100, 3)$, having relatively high swirl strengths and which are asymptotically stable when considered individually. Taking axial wavenumber k and time horizon τ as independent variables, contours of maximum transient energy growth were obtained. Global maximum transient energy growth of $G_{max} = 1.45 \times 10^4$ occurs for time horizons equivalent to the merging phase, around $\tau \approx 39$. The spatial distribution of the optimal initial conditions was similar to the $q = 2$ study and involved energy in the interaction region between the two cores and the outer circular regions of the two base flow cores.

Over shorter time horizons the co-rotating vortex pair underwent transient growth mechanisms similar to that observed for the isolated vortex as discussed by Antkowiak & Brancher (2004). These mechanisms involved either Orr-type unfolding followed by an induction of base flow vorticity when $k = 0$, or through a resonance effect when $k = 0.75$ (see also Pradeep & Hussain 2006). However, for longer time horizons the transient growths significantly exceed those for the isolated vortices, and in the $k = 0$ case this was attributed to a rotationally symmetric optimal initial condition that allowed for continued core-induction while maintaining the symmetry of the base flow merging system. In contrast, when $k = 0.75$ we conjecture, based on similarities to features observed in the (quasi-steady) asymptotic stability investigation of Roy *et al.* (2008), that elliptic instability is present before merging occurs.

In §§ 5.2 and 5.3, when the initial vortex flows were asymptotically stable/weakly unstable, the optimal perturbations for both an isolated vortex and a co-rotating vortex pair took the form of partial vortex rings. Similar structures of optimal initial perturbations have been reported in the context of a counter-rotating vortex pair by Brion, Sipp & Jacquin (2007), who suggested that the optimal perturbations to any compact distribution of vorticity will have the form of one or several partial vortex rings around it.

DNS of stable base flow (with $Re, q = 100, 3$) seeded with the optimal initial perturbation obtained from the linearized analysis was also undertaken (§ 6). It was shown that the optimal two-dimensional perturbation at $k = 0$ induces a dual vortex meandering, that is, the vortices are driven towards each other and so the vortex merging is accelerated or driven away from each other so the vortex merging is delayed, depending on the sign of the initial perturbation. Nonlinear development of the optimal perturbation at $k = 0.75$, where the transient growth reaches a global maximum for the pair system, is observed to drive the vortex pair to break up before merging.

Acknowledgements

We would like to thank K. Ryan for his helpful discussions with us. X.M. would like to acknowledge the Student Opportunity Fund at Imperial College London for financial support while S.J.S. wishes also to acknowledge financial support from EPSRC grants EP/H000208/1 and EP/H050507/1. H.M.B. is grateful for

https://doi.org/10.1017/jfm.2012.171 Published online by Cambridge University Press

support obtained through the Australian National Computational Infrastructure Merit Allocation Scheme, grant D77, and from the Australian Research Council through grant DP1096444.

REFERENCES

ANTKOWIAK, A. & BRANCHER, P. 2004 Transient energy growth for the Lamb–Oseen vortex. *Phys. Fluids* **16** (1) L1–4.

ANTKOWIAK, A. & BRANCHER, P. 2007 On vortex rings around vortices: an optimal mechanism. *J. Fluid Mech.* **578**, 295–304.

BARKLEY, D., BLACKBURN, H. M. & SHERWIN, S. J. 2008 Direct optimal growth analysis for time steppers. *Intl J. Numer. Meth. Fluids* **57**, 1437–1458.

BATCHELOR, G. K. 1964 Axial flow in trailing line vortices. *J. Fluid Mech.* **20**, 645–658.

BLACKBURN, H. M., BARKLEY, D. & SHERWIN, S. J. 2008 Convective instability and transient growth in flow over a backward-facing step. *J. Fluid Mech.* **603**, 271–304.

BRION, V., SIPP, D. & JACQUIN, L. 2007 Optimal amplification of the Crow instability. *Phys. Fluids* **19**, 111703–1–XX.

BROADHURST, M. S. 2007 Vortex stability and breakdown: direct numerical simulation and stability analysis using biglobal and parabolised formulations. PhD thesis, Department of Aeronautics, Imperial College London.

CROUCH, J. 2005 Airplane trailing vortices and their control. *C. R. Physique* **6**, 487–499.

CROW, S. C. 1970 Stability theory for a pair of trailing vortices. *AIAA J.* **8**, 2172–2179.

DONNADIEU, C., ORTIZ, S., CHOMAZ, J.-M. & BILLANT, P. 2009 Three-dimensional instabilities and transient growth of a counter-rotating vortex pair. *Phys. Fluids* **21**.

FABRE, D. & JACQUIN, L. 2004 Viscous instabilities in trailing vortices at large swirl numbers. *J. Fluid Mech.* **500**, 239–262.

FABRE, D., SIPP, D. & JACQUIN, L. 2006 Kelvin waves and the singular modes of the Lamb–Oseen vortex. *J. Fluid Mech.* **551**, 235–274.

GUERMOND, J. L., MINEV, P. & SHEN, J. 2006 An overview of projection methods for incompressible flows. *Comput. Meth. Appl. Mech. Engng* **195**, 6011–6045.

HEATON, C. J. 2007*a* Centre modes in inviscid swirling flows and their application to the stability of the Batchelor vortex. *J. Fluid Mech.* **576**, 325–348.

HEATON, C. J. 2007*b* Optimal growth of the Batchelor vortex viscous modes. *J. Fluid Mech.* **592**, 495–505.

HEATON, C. J. & PEAKE, N. 2007 Transient growth in vortices with axial flow. *J. Fluid Mech.* **587**, 271–301.

HUSSAIN, F., PRADEEP, D. S. & STOUT, E. 2011 Nonlinear transient growth in a vortex column. *J. Fluid Mech.* **682**, 304–331.

JIMÉNEZ, J. 1975 Stability of a pair of co-rotating vortices. *Phys. Fluids* **18** (11), 1580–1581.

KARNIADAKIS, G. E., ISRAELI, M. & ORSZAG, S. A. 1991 High-order splitting methods for the incompressible Navier–Stokes equations. *J. Comput. Phys.* **97** (2), 414–443.

KERSWELL, R. R. 2002 Elliptic instability. *Annu. Rev. Fluid Mech.* **34**, 83–113.

KHORRAMI, M. R. 1991 On the viscous modes of instability of a trailing line vortex. *J. Fluid Mech.* **225**, 197–212.

LACAZE, L., RYAN, K. & LE DIZÈS, S. 2007 Elliptic instability in a strained Batchelor vortex. *J. Fluid Mech.* **577**, 341–361.

LE DIZÈS, S. & FABRE, D. 2007 Large-Reynolds-number asymptotic analysis of viscous centre modes in vortices. *J. Fluid Mech.* **585**, 153–180.

LE DIZÈS, S. & LAPORTE, F. 2002 Theoretical predictions for the elliptical instability in a two-vortex flow. *J. Fluid Mech.* **471**, 169–201.

LE DIZÈS, S. & VERGA, A. 2002 Viscous interactions of two co-rotating vortices before merging. *J. Fluid Mech.* **467**, 389–410.

LESSEN, M. & PAILLET, F. 1974 The stability of a trailing line vortex. Part 2. Viscous theory. *J. Fluid Mech.* **65**, 769–779.

https://doi.org/10.1017/jfm.2012.171 Published online by Cambridge University Press

LESSEN, M., SINGH, P. J. & PAILLET, F. 1974 The stability of a trailing line vortex. Part 1. Inviscid theory. *J. Fluid Mech.* **63**, 753–763.

MAO, X. 2010 Vortex instability and transient growth. PhD thesis, Imperial College London.

MAO, X. & SHERWIN, S. J. 2012 Transient growth associated with continuous spectra of the Batchelor vortex. *J. Fluid Mech.* **697**, 35–59.

MAO, X., SHERWIN, S. J. & BLACKBURN, H. M. 2011 Transient growth and bypass transition in stenotic flow with a physiological waveform. *Theor. Comput. Fluid Dyn.* **25** (1), 31–42.

MAYER, E. W. & POWELL, K. G. 1992 Viscous and inviscid instabilities of a trailing vortex. *J. Fluid Mech.* **245**, 91–114.

MEUNIER, P., LE DIZÈS, S. & LEWEKE, T. 2005 Physics of vortex merging. *C. R. Physique* **6**, 431–450.

MEUNIER, P. & LEWEKE, T. 2005 Elliptic instability of a co-rotating vortex pair. *J. Fluid Mech.* **533**, 125–159.

MOORE, D. W. & SAFFMAN, P. G. 1975 The instability of a straight vortex filament in a strain field. *Proc. R. Soc. Lond.* A **346**, 413–425.

PRADEEP, D. S. & HUSSAIN, F. 2006 Transient growth of perturbations in a vortex column. *J. Fluid Mech.* **550**, 251–288.

ROY, C., SCHAEFFER, N., LE DIZÈS, S. & THOMPSON, M. C. 2008 Stability of a pair of co-rotating vortices with axial flow. *Phys. Fluids* **20** (9)094101.

SIPP, D., JACQUIN, L. & COSSU, C. 2000 Self-adaptation and viscous selection in concentrated two-dimensional dipoles. *Phys. Fluids* **12**, 245–248.

STEWARTSON, K. & BROWN, S. N. 1985 Near-neutral centre-modes as inviscid perturbations to a trailing line vortex. *J. Fluid Mech.* **156**, 387–399.

TSAI, C. & WIDNALL, S. 1976 The stability of short waves on a straight vortex filament in a weak externally imposed strain field. *J. Fluid Mech.* **73**, 721–733.

TUCKERMAN, L. S. & BARKLEY, D. 2000 Bifurcation analysis for time steppers. In *Numerical Methods for Bifurcation Problems and Large-Scale Dynamical Systems* (ed. E. Doedel & L. S. Tuckerman). pp. 453–566. Springer.

https://doi.org/10.1017/jfm.2012.171 Published online by Cambridge University Press